

INTERNATIONAL JOURNAL FOR NUMERICAL METHODS IN ENGINEERING

Int. J. Numer. Meth. Engng 2006; **68**:231–266

Published online 30 March 2006 in Wiley InterScience (www.interscience.wiley.com). DOI: 10.1002/nme.1710

Continuum-based design sensitivity analysis and optimization of nonlinear shell structures using meshfree method

Kiyong Yi^{1,‡}, K. K. Choi^{1,*}, Nam H. Kim^{2,¶} and Mark E. Botkin^{3,||}¹*Department of Mechanical and Industrial Engineering, The University of Iowa, Iowa City, IA 52242, U.S.A.*²*Department of Mechanical and Aerospace Engineering, University of Florida, Gainesville, FL 32611, U.S.A.*³*Vehicle Development Research Lab, GM R&D and Strategic Planning, Warren, MI 48090, U.S.A.*

SUMMARY

A continuum-based shape and configuration design sensitivity analysis (DSA) method for a finite deformation elastoplastic shell structure has been developed. Shell elastoplasticity is treated using the projection method that performs the return mapping on the subspace defined by the zero-normal stress condition. An incrementally objective integration scheme is used in the context of finite deformation shell analysis, wherein the stress objectivity is preserved for finite rotation increments. The material derivative concept is used to develop a continuum-based shape and configuration DSA method. Significant computational efficiency is obtained by solving the design sensitivity equation without iteration at each converged load step using the same consistent tangent stiffness matrix. Numerical implementation of the proposed shape and configuration DSA is carried out using the meshfree method. The accuracy and efficiency of the proposed method is illustrated using numerical examples. Copyright © 2006 John Wiley & Sons, Ltd.

KEY WORDS: continuum-based design sensitivity analysis; nonlinear shell structure; design optimization; finite deformation; elastoplasticity; meshfree method

1. INTRODUCTION

Shell structures are frequently used in the construction of aerospace, automotive, and civil engineering structures. A significant amount of effort has been put into the design sensitivity analysis (DSA) and optimization of shell structures [1–12]. Yamazaki and Vandeplaats [3]

*Correspondence to: K. K. Choi, Department of Mechanical and Industrial Engineering, The University of Iowa, Iowa City, IA 52242, U.S.A.

†E-mail: kkchoi@ccad.uiowa.edu

‡Graduate Research Assistant.

§Roy J. Carver Professor.

¶Assistant Professor.

||Principal Research Engineer.

Contract/grant sponsor: General Motors Corporation

Received 19 September 2005

Revised 11 February 2006

Accepted 11 February 2006

Copyright © 2006 John Wiley & Sons, Ltd.

performed sizing and shape DSA of isoparametric shell element using the discrete method. Linby and Santos [7] proposed method for shape optimization of a shell structure that is parameterized using a CAD system and discrete method. Moita *et al.* [8] performed DSA of a triangular flat plate finite element considering geometric nonlinearity. Choi *et al.* [9] performed shape and topology optimization for locating the best positions of joining mechanisms using a doubly curved shell. In this paper, a continuum-based shape and configuration DSA method for a finite deformation elastoplastic shell structure is developed.

In the literature, three approaches for DSA have been used for a shell structure: the finite difference method (FDM), the discrete method, and the continuum-based method. Because FDM is the simplest method, it is frequently used to optimize shell structures. However, it lacks accuracy and involves high computational costs. On the other hand, in the discrete DSA method, the approximated matrix equation is differentiated, and thus the method has difficulty in obtaining derivatives of numerically constructed stiffness matrices. In the continuum-based DSA method, the variational equation is differentiated before discretization. Therefore, the continuum-based DSA method is more efficient and can circumvent the inaccuracy that is associated with differentiation of the approximated matrix equation in discrete DSA, although it requires lengthy analytical derivations. In this paper, a continuum-based shape and configuration DSA method for a finite deformation elastoplastic shell structure is developed.

In the continuum-based DSA, the design sensitivity equation can be discretized using any numerical method such as finite element method (FEM) or meshfree method. In this paper, a meshfree method is used to discretize design sensitivity equation. The meshfree method is an ideal choice in shape and configuration optimization of the nonlinear shell structure since, compared with FEM, the solution is much less sensitive to the mesh distortion, which could occur during shape design change and finite deformation nonlinear analysis. More information of the meshfree discretization of shell structures can be obtained from Kim *et al.* [12] where they proposed a continuum-based design sensitivity formulation for the linear shell structures using the meshfree method. Since no element information is generated in the meshfree method, surface information from the CAD geometry is necessary for constructing the surface normal vector and a mapping from the global to local coordinate, both of which are essential in representing the general curved shell structure. In nonlinear shell analysis, the normal vector and mapping must be updated using the rotational response at the current configuration in order to account for the finite rotation increment. Another distinction between the linear and nonlinear shell structures lies in the integration through the thickness. Given the assumption of a constant transverse shear deformation, an analytical integration can be performed through the thickness coordinate in linear shell structures, whereas a numerical integration through thickness coordinate should be carried out to capture plastic deformation in nonlinear shell structures.

The most widely used integration procedure for plane strain and three-dimensional elastoplastic analysis is the radial return mapping algorithm. Since the return mapping algorithm is strain driven, three-dimensional return mapping algorithms can be easily modified for the plane strain problem. Shell elastoplastic integration, however, is nontrivial because of its zero normal stress condition. There are two approaches: the iterative method with a zero normal stress condition, which is based on the use of the three-dimensional plasticity model, and the projection method, which performs return mapping on the subspace defined by the plane stress condition proposed by Simo and Taylor [13] and Simo and Kennedy [14].

Among several incrementally objective integration schemes in finite deformation analysis, in which stress objectivity is preserved for finite rotation increments, the Hughes–Winget algorithm

[15–17] is used in this paper. This algorithm is used for DSA because any formulation of the tangent stiffness matrix, which is critical for efficient DSA that is consistent with other integration scheme is not yet available. In addition, the Hughes–Winget algorithm provides the possibility of using an existing small-strain shell elastoplastic integration procedure without modification.

The organization of this paper is as follows. In Section 2, the CAD geometry-based shell kinematic is explained. The nonlinear variational equation of finite deformation elastoplastic shell structure is presented in Section 3. The continuum-based DSA method is developed in Section 4. A meshfree discretization is presented in Section 5, followed by numerical examples of DSA and optimization in Section 6, where the accuracy and efficiency of the proposed method is shown.

2. CAD GEOMETRY-BASED SHELL KINEMATICS

A general shell structure is represented by the thickness and neutral surface as shown in Figure 1(a)–(c). Figure 1(c) and (d) show the neutral surface geometry and its transformation (mapping) into the parametric coordinate, respectively. A neutral surface can be constructed by using the CAD geometry data. In the CAD tool, a general neutral surface geometry in a three-dimensional space can be represented by using two parameters as [18, 19]

$$\mathbf{x}^n(\xi, \eta) = \mathbf{U}(\xi)^T \mathbf{M} \mathbf{G} \mathbf{M}^T \mathbf{W}(\eta) \quad (1)$$

where $\mathbf{U}(\xi) = [\xi^3, \xi^2, \xi, 1]^T$ and $\mathbf{W}(\eta) = [\eta^3, \eta^2, \eta, 1]^T$ are vectors in the parametric coordinates, and the superscript n denotes the point on the neutral surface. In (1), \mathbf{M} is the matrix defined as

$$\mathbf{M} = \begin{bmatrix} 2 & -2 & 1 & 1 \\ -3 & 3 & -2 & -1 \\ 0 & 0 & 1 & 0 \\ 1 & 0 & 0 & 0 \end{bmatrix} \quad (2)$$

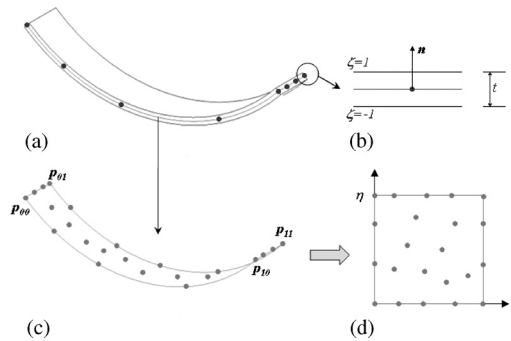


Figure 1. Shell structure.

and \mathbf{G} is the surface geometric matrix defined as

$$\mathbf{G} = \begin{bmatrix} \mathbf{p}_{00} & \mathbf{p}_{01} & \mathbf{p}_{00}^{\eta} & \mathbf{p}_{01}^{\eta} \\ \mathbf{p}_{10} & \mathbf{p}_{11} & \mathbf{p}_{10}^{\eta} & \mathbf{p}_{11}^{\eta} \\ \mathbf{p}_{00}^{\xi} & \mathbf{p}_{01}^{\xi} & \mathbf{p}_{00}^{\xi\eta} & \mathbf{p}_{01}^{\xi\eta} \\ \mathbf{p}_{10}^{\xi} & \mathbf{p}_{11}^{\xi} & \mathbf{p}_{10}^{\xi\eta} & \mathbf{p}_{11}^{\xi\eta} \end{bmatrix}_{4 \times 4 \times 3} \quad (3)$$

where \mathbf{p}_{ij} are coordinates of the corner points on the surface, \mathbf{p}_{ij}^{ξ} and \mathbf{p}_{ij}^{η} are the tangent vectors in ξ and η directions, and $\mathbf{p}_{ij}^{\xi\eta}$ are the twist vectors.

The normal vector of the shell can be obtained from the neutral surface representation as

$$\mathbf{n}(\xi, \eta) = \frac{\mathbf{x}_{,\xi}^n \times \mathbf{x}_{,\eta}^n}{\|\mathbf{x}_{,\xi}^n \times \mathbf{x}_{,\eta}^n\|} \quad (4)$$

where, from (1)

$$\mathbf{x}_{,\xi}^n = \mathbf{U}_{,\xi}^T(\xi) \mathbf{M} \mathbf{G} \mathbf{M}^T \mathbf{W}(\eta) \quad (5)$$

$$\mathbf{x}_{,\eta}^n = \mathbf{U}(\xi)^T \mathbf{M} \mathbf{G} \mathbf{M}^T \mathbf{W}_{,\eta}(\eta) \quad (6)$$

For the shell structure with thickness $t(\xi, \eta)$, any points within the structure can be expressed by

$$\mathbf{x}(\xi, \eta, \zeta) = \mathbf{U}(\xi)^T \mathbf{M} \mathbf{G} \mathbf{M}^T \mathbf{W}(\eta) + \zeta \frac{t}{2} \mathbf{n}(\xi, \eta) \quad (7)$$

where $\zeta = [-1, 1]$ is the third parametric coordinate in the thickness direction, and $\mathbf{n}(\xi, \eta)$ is the outward unit vector of the surface that is obtained from (4). The Jacobian of the mapping between physical and parametric coordinate can be obtained from (7) as

$$\begin{aligned} \mathbf{x}_{,\xi} &= \mathbf{U}_{,\xi}^T \mathbf{M} \mathbf{G} \mathbf{M}^T \mathbf{W} + \zeta \frac{t}{2} \mathbf{n}_{,\xi} \\ \mathbf{x}_{,\eta} &= \mathbf{U}^T \mathbf{M} \mathbf{G} \mathbf{M}^T \mathbf{W}_{,\eta} + \zeta \frac{t}{2} \mathbf{n}_{,\eta} \\ \mathbf{x}_{,\zeta} &= \frac{t}{2} \mathbf{n} \end{aligned} \quad (8)$$

The notations $\mathbf{x} = [x, y, z]^T \equiv [x_1, x_2, x_3]^T$ and $\xi = [\xi, \eta, \zeta]^T \equiv [\xi_1, \xi_2, \xi_3]^T$ will be used in the following derivations. Using these notations, the Jacobian of the mapping can be represented by

$$\mathbf{J} = \frac{\partial x_i}{\partial \xi_j} \quad (9)$$

For the shell structure, the constitutive relation is given in the body-fixed, local coordinate, whereas a displacement–strain relation is provided in the global coordinate. The unit vectors in the local coordinate are calculated as

$$\mathbf{l} = \frac{\mathbf{x}_{,\xi}^n}{\|\mathbf{x}_{,\xi}^n\|}, \quad \mathbf{n} = \frac{\mathbf{x}_{,\xi}^n \times \mathbf{x}_{,\eta}^n}{\|\mathbf{x}_{,\xi}^n \times \mathbf{x}_{,\eta}^n\|}, \quad \mathbf{m} = \mathbf{n} \times \mathbf{l} \quad (10)$$

Using the relation in (10), the coordinate transformation can be obtained as

$$\mathbf{x} = \begin{bmatrix} l_1 & m_1 & n_1 \\ l_2 & m_2 & n_2 \\ l_3 & m_3 & n_3 \end{bmatrix} \mathbf{x}' \quad (11)$$

where \mathbf{x}' is the global coordinate of the corresponding point \mathbf{x} in the local coordinate.

In the shell analysis, the flat cross-section remains flat during deformation. Thus, the displacement varies linearly in the thickness direction; and can be represented by the addition of two terms as

$$\mathbf{z} = \mathbf{z}^1(\xi, \eta) + \zeta \mathbf{z}^2(\xi, \eta) \quad (12)$$

where $\mathbf{z}^1(\xi, \eta)$ represents the incremental displacement of the neutral surface and $\zeta \mathbf{z}^2(\xi, \eta)$ denotes the incremental rotation of the cross-section.

The strain tensor can be expressed as

$$\varepsilon_{ij}(\mathbf{z}) = \frac{1}{2} \left(\frac{\partial z_i}{\partial x_j} + \frac{\partial z_j}{\partial x_i} \right) = \frac{1}{2} \left(\frac{\partial z_i}{\partial \xi_m} \frac{\partial \xi_m}{\partial x_j} + \frac{\partial z_j}{\partial \xi_m} \frac{\partial \xi_m}{\partial x_i} \right) \quad (13)$$

where the summation convention is used for repeated indices. Similar to the displacement, the strain tensor in (13) can also be represented by the addition of two terms

$$\varepsilon_{ij}(\mathbf{z}) = \varepsilon_{ij}^1(\mathbf{z}) + \zeta \varepsilon_{ij}^2(\mathbf{z}) \quad (14)$$

where

$$\varepsilon_{ij}^1(\mathbf{z}) = \frac{1}{2} \left(\frac{\partial z_i^1}{\partial \xi_m} J_{mj}^{-1} + \frac{\partial z_j^1}{\partial \xi_m} J_{mi}^{-1} + z_i^2 J_{3j}^{-1} + z_j^2 J_{3i}^{-1} \right) \quad (15)$$

and

$$\varepsilon_{ij}^2(\mathbf{z}) = \frac{1}{2} \left(\frac{\partial z_i^2}{\partial \xi_m} J_{mj}^{-1} + \frac{\partial z_j^2}{\partial \xi_m} J_{mi}^{-1} \right) \quad (16)$$

are the membrane–shear strain and bending strain, respectively. In the finite rotation nonlinear shell problem, the strain tensor is calculated at the midpoint configuration to obtain a second-order accuracy, which will be explained in the following section.

3. VARIATIONAL EQUATION OF FINITE DEFORMATION ELASTOPLASTIC SHELL STRUCTURE

3.1. Shell elastoplastic analysis

A brief review of shell elastoplastic analysis is presented to introduce notations that appear in the following DSA section. One complexity in the shell elastoplastic analysis is that the plastic evolution appears in deviatoric space, while the zero normal stress condition is imposed in stress space. The deviatoric stress $\tilde{\mathbf{s}}$ is defined using the Cauchy stress $\tilde{\boldsymbol{\sigma}}$ as

$$\tilde{\mathbf{s}} = \begin{bmatrix} s_{11} & s_{12} & s_{13} \\ s_{21} & s_{22} & s_{23} \\ s_{31} & s_{32} & s_{33} \end{bmatrix} = \begin{bmatrix} \sigma_{11} & \sigma_{12} & \sigma_{13} \\ \sigma_{21} & \sigma_{22} & \sigma_{23} \\ \sigma_{31} & \sigma_{32} & \sigma_{33} \end{bmatrix} - \frac{(\sigma_{11} + \sigma_{22} + \sigma_{33})}{3} \begin{bmatrix} 1 & 0 & 0 \\ 0 & 1 & 0 \\ 0 & 0 & 1 \end{bmatrix} \quad (17)$$

Let V^S be the vector space of symmetric order-2 stress tensors. Thus, $\dim V^S = 6$. The shell stress subspace V^P is obtained by imposing the zero normal stress condition as

$$V^P \equiv \{\boldsymbol{\sigma} \in V^S | \sigma_{33} = 0\} \quad (18)$$

Similarly, the corresponding deviatoric subspace V^D is defined as

$$V^D \equiv \{\mathbf{s} \in V^S | s_{kk} = 0\} \quad (19)$$

Therefore, $\dim V^P = \dim V^D = 5$. Vector notations are employed to represent each vector as

$$\boldsymbol{\sigma} = [\sigma_{11} \ \sigma_{22} \ \sigma_{12} \ \sigma_{23} \ \sigma_{31}]^T \quad (20)$$

$$\mathbf{s} = [s_{11} \ s_{22} \ s_{12} \ s_{23} \ s_{31}]^T \quad (21)$$

Although s_{33} is not included in (21), it is nonzero and can be calculated from the constraint $s_{kk} = 0$. Since the imposition of the zero normal stress constraint is not straightforward in the deviatoric subspace, the mapping relation between $\boldsymbol{\sigma} \in V^P$ and $\mathbf{s} \in V^D$ is required. In matrix form it is

$$\mathbf{s} = \bar{\mathbf{P}}\boldsymbol{\sigma}, \quad \bar{\mathbf{P}} = \frac{1}{3} \begin{bmatrix} 2 & -1 & 0 & 0 & 0 \\ -1 & 2 & 0 & 0 & 0 \\ 0 & 0 & 3 & 0 & 0 \\ 0 & 0 & 0 & 3 & 0 \\ 0 & 0 & 0 & 0 & 3 \end{bmatrix} \quad (22)$$

Using the same mapping matrix, the back stress $\boldsymbol{\alpha} \in V^P$ and its deviatoric part $\boldsymbol{\alpha}' \in V^D$ is related by

$$\boldsymbol{\alpha}' = \bar{\mathbf{P}}\boldsymbol{\alpha} \quad (23)$$

The strain tensor can be expressed as in (13)

$$\varepsilon_{ij}(z) = \frac{1}{2} \left(\frac{\partial z_i}{\partial x_j} + \frac{\partial z_j}{\partial x_i} \right) \quad (24)$$

Since the vector notations are used to represent the stress, the strains also need to be expressed in vector notation. They have a dimension of five and take the vector form of

$$\boldsymbol{\varepsilon} = [\varepsilon_{11} \ \varepsilon_{22} \ 2\varepsilon_{12} \ 2\varepsilon_{23} \ 2\varepsilon_{31}]^T \quad (25)$$

$$\boldsymbol{\varepsilon}^p = [\varepsilon_{11}^p \ \varepsilon_{22}^p \ 2\varepsilon_{12}^p \ 2\varepsilon_{23}^p \ 2\varepsilon_{31}^p]^T \quad (26)$$

From small elastic strain and small rigid-body rotation assumptions, the strain and its rate can be additively decomposed into elastic and plastic part as

$$\boldsymbol{\varepsilon} = \boldsymbol{\varepsilon}^e + \boldsymbol{\varepsilon}^p, \quad \dot{\boldsymbol{\varepsilon}} = \dot{\boldsymbol{\varepsilon}}^e + \dot{\boldsymbol{\varepsilon}}^p \quad (27)$$

The constitutive equation is written as

$$\boldsymbol{\sigma} = \mathbf{D}\boldsymbol{\varepsilon}^e \quad (28)$$

where \mathbf{D} is the elastic constitutive matrix after enforcing zero normal stress constraint.

In rate-independent plasticity, the von Mises yield criterion with an associative flow rule is the well-known method, which is used in this paper. Accordingly, the yield function is defined as

$$f \equiv \frac{1}{2} \boldsymbol{\eta}^T \mathbf{P} \boldsymbol{\eta} - \frac{1}{3} \kappa^2 (\bar{\varepsilon}^p) \leq 0 \quad (29)$$

where $\boldsymbol{\eta} \equiv \boldsymbol{\sigma} - \boldsymbol{\alpha}$; $\kappa(\bar{\varepsilon}^p)$ is the radius of the yield surface, which is determined by the isotropic hardening rule; and \mathbf{P} is the mapping matrix modified from $\bar{\mathbf{P}}$ in order to account for the factor of two in the shear strain component, written as

$$\mathbf{P} \equiv \frac{1}{3} \begin{bmatrix} 2 & -1 & 0 & 0 & 0 \\ -1 & 2 & 0 & 0 & 0 \\ 0 & 0 & 6 & 0 & 0 \\ 0 & 0 & 0 & 6 & 0 \\ 0 & 0 & 0 & 0 & 6 \end{bmatrix} \quad (30)$$

In the following, a linearly combined isotropic–kinematic hardening rule is used as

$$\kappa(\bar{\varepsilon}^p) = \sigma_0 + \beta H \bar{\varepsilon}^p \quad (31)$$

where $\bar{\varepsilon}^p$ is an effective plastic strain; β is one when the pure isotropic hardening rule is used, and zero when the pure kinematic hardening rule is used; σ_0 is the initial yield stress; and H is the hardening parameter. The back stress can be determined by the kinematic hardening rule as

$$\dot{\boldsymbol{\alpha}} = \frac{2}{3} \lambda (1 - \beta) H \boldsymbol{\eta} \quad (32)$$

where λ is a plastic consistency parameter, which is zero when the material is in the elastic status and positive when it is in the plastic status. In this section only, the superposed dot will be used to denote the rate of the variable, whereas in the rest of the paper, it denotes the material derivative (see Section 4). Since the associative flow rule is used, the plastic strain is proportional to the normal of the yield surface. Thus,

$$\dot{\boldsymbol{\varepsilon}}^p = \lambda \mathbf{P} \boldsymbol{\eta} \quad (33)$$

The rate of effective plastic strain can be expressed as

$$\dot{e}^p = \sqrt{\frac{2}{3}} \lambda \phi \quad (34)$$

where $\phi = [\boldsymbol{\eta}^T \mathbf{P} \boldsymbol{\eta}]^{1/2}$. Loading/unloading conditions can be formulated using the Kuhn–Tucker condition as

$$f \leq 0, \quad \lambda \geq 0, \quad \lambda f = 0 \quad (35)$$

where the nonpositive property of the yield function is regarded as an inequality constraint and the plastic consistency parameter λ as the corresponding Lagrange multiplier.

3.2. Numerical integration procedure for shell elastoplastic analysis

The basic problem of integrating elastoplastic constitutive equations can be stated as follows. On the time interval of interest $[0, T]$, it is assumed that at time t_n the total and plastic strain fields and the back stress field are all known; that is,

$$\{ {}^n \boldsymbol{\varepsilon}, {}^n \boldsymbol{\varepsilon}^p, {}^n \bar{e}^p, {}^n \boldsymbol{\alpha} \} \text{ are known fields at time } t_n \quad (36)$$

In the displacement-driven solution procedure, the incremental displacement field over the time step $[t_n, t_{n+1}]$ is available, from which the incremental strain $\Delta \boldsymbol{\varepsilon}$ can be calculated. From additive decomposition, the strain at time t_{n+1} can be calculated by

$${}^{n+1} \boldsymbol{\varepsilon} = {}^n \boldsymbol{\varepsilon} + \Delta \boldsymbol{\varepsilon} \quad (37)$$

The remaining independent variables must be updated using the integration algorithm. A standard backward Euler method is used to integrate the rate-form elastoplastic equations. First, it is assumed that the incremental strain is elastic, which means that all plastic variables remain fixed. Using the subscript ‘tr’ to denote the trial status, the following relations are obtained:

$$\begin{aligned} \boldsymbol{\varepsilon}_{\text{tr}}^p &= {}^n \boldsymbol{\varepsilon}^p \\ \boldsymbol{\alpha}_{\text{tr}} &= {}^n \boldsymbol{\alpha} \\ \bar{e}_{\text{tr}}^p &= {}^n \bar{e}^p \\ \boldsymbol{\sigma}_{\text{tr}} &= \mathbf{D}({}^{n+1} \boldsymbol{\varepsilon} - {}^n \boldsymbol{\varepsilon}) \\ \boldsymbol{\eta}_{\text{tr}} &= \boldsymbol{\sigma}_{\text{tr}} - \boldsymbol{\alpha}_{\text{tr}} \end{aligned} \quad (38)$$

Using this trial status, the yield function in (29) is evaluated. If $f \leq 0$, then the trial status is the final status and the material is in the elastic range.

Otherwise the material is in the plastic range, and return mapping is performed to find the nonnegative consistency parameter $\Delta\lambda = \lambda\Delta t$, which makes the yield function vanish, i.e. $f(\Delta\lambda) = 0$. The backward Euler integration algorithm of the rate-form evolution equations can be written as

$$\begin{aligned} {}^{n+1}\boldsymbol{\varepsilon}^p &= {}^n\boldsymbol{\varepsilon}^p + \Delta\lambda \mathbf{P} {}^{n+1}\boldsymbol{\eta} \\ {}^{n+1}\boldsymbol{\alpha} &= {}^n\boldsymbol{\alpha} + \frac{2}{3}\Delta\lambda(1-\beta)H {}^{n+1}\boldsymbol{\eta} \\ {}^{n+1}\bar{\boldsymbol{\varepsilon}}^p &= {}^n\bar{\boldsymbol{\varepsilon}}^p + \sqrt{\frac{2}{3}}\Delta\lambda {}^{n+1}\phi \\ {}^{n+1}\boldsymbol{\sigma} &= \mathbf{D}({}^{n+1}\boldsymbol{\varepsilon} - {}^{n+1}\boldsymbol{\varepsilon}^p) \\ {}^{n+1}\boldsymbol{\eta} &= {}^{n+1}\boldsymbol{\sigma} - {}^{n+1}\boldsymbol{\alpha} \end{aligned} \quad (39)$$

The plastic consistency parameter $\Delta\lambda$ is obtained by enforcing the plastic consistency condition at t_{n+1} . After inserting the relations in the above equation into (29) with $f = 0$, the consistency condition is written in the form

$${}^{n+1}\phi = \sqrt{\frac{2}{3}}[{}^0\sigma + \beta H {}^n\bar{\boldsymbol{\varepsilon}}^p] + \frac{2}{3}\beta H \Delta\lambda {}^{n+1}\phi \quad (40)$$

The above equation is a nonlinear algebraic equation, which is solved for $\Delta\lambda$ using the Newton–Raphson iterative method. After solving $\Delta\lambda$ from (40), all independent variables in (39) are updated at time t_{n+1} . The integration algorithm in (39) preserves the zero normal stress condition.

3.3. Finite deformation shell analysis

The theories involving various objective rates of rotational type can be cast into a uniform format, form identical to small deformation theory. They take on canonically simple forms when transformed to rotation-free configuration. Therefore, the way that the finite incremental rotation is evaluated is the key difference between these schemes. Among the several incrementally objective integration schemes, the Hughes–Winget algorithm is used in this paper. The algorithm is summarized as

$${}^{n+1}\sigma_{ij}^g = r_{ik} {}^n\sigma_{kl}^g r_{jl} + \Delta\sigma_{ij}^g \quad (41)$$

where the second term on the right side represents the material response and is determined by the numerical integration procedure presented in the previous section, whereas the first term accounts for rotational effects, and where r_{ij} is defined using the midpoint rule as

$$r_{ij} = \delta_{ij} + (\delta_{ik} - \frac{1}{2}\Delta\omega_{ik})^{-1}\Delta\omega_{kj} \quad (42)$$

In (41), the superscript ‘g’ denotes the quantity in the global coordinate. The strain and rotational increments are calculated at the midpoint configuration to obtain a second-order accuracy as

$$\Delta \varepsilon_{ij}^g = \frac{1}{2} \left(\frac{\partial \Delta z_i}{\partial^{n+(1/2)} x_j} + \frac{\partial \Delta z_j}{\partial^{n+(1/2)} x_i} \right) \quad (43)$$

$$\Delta \omega_{ij} = \frac{1}{2} \left(\frac{\partial \Delta z_i}{\partial^{n+(1/2)} x_j} - \frac{\partial \Delta z_j}{\partial^{n+(1/2)} x_i} \right) \quad (44)$$

where ${}^{n+(1/2)}x_i = {}^n x_i + \frac{1}{2} \Delta z_i$.

If the global stress vector is defined as

$$\boldsymbol{\sigma}^g \equiv [\sigma_{11} \ \sigma_{12} \ \sigma_{13} \ \sigma_{21} \ \sigma_{22} \ \sigma_{23} \ \sigma_{31} \ \sigma_{32} \ \sigma_{33}]^T \quad (45)$$

then (41) can be written in vector notation as

$${}^{n+1} \boldsymbol{\sigma}^g = \mathbf{R} {}^n \boldsymbol{\sigma}^g + \Delta \boldsymbol{\sigma}^g \quad (46)$$

where \mathbf{R} is the 9×9 rotational matrix defined as $R_{ijkl} = r_{ik} r_{jl}$.

The key advantage of the Hughes–Winget algorithm is the ability to use the small deformation integration procedure introduced in the previous section where the stress vector is defined in body-fixed local coordinate. The global stress can be transformed to the local stress by using the 9×9 transformation matrix as

$${}^{n+1} \boldsymbol{\sigma}^l = {}^{n+1} \mathbf{Q} {}^{n+1} \boldsymbol{\sigma}^g, \quad {}^{n+1} \boldsymbol{\sigma}^g = {}^{n+1} \mathbf{Q}^T {}^{n+1} \boldsymbol{\sigma}^l \quad (47)$$

where the global-to-local transformation matrix at current configuration ${}^{n+1} \mathbf{Q}$ must be updated consistently using the finite deformation integration algorithm as

$${}^{n+1} \mathbf{Q}^T = \mathbf{R} {}^n \mathbf{Q}^T, \quad {}^{n+1} \mathbf{Q} = {}^n \mathbf{Q} \mathbf{R}^T \quad (48)$$

The initial global-to-local transformation matrix ${}^0 \mathbf{Q}$ is constructed using three local vectors in (10) as

$${}^0 \mathbf{Q} = \begin{bmatrix} l_1^2 & l_1 m_1 & l_1 n_1 & m_1 l_1 & m_1^2 & m_1 n_1 & n_1 l_1 & n_1 m_1 & n_1^2 \\ l_1 l_2 & l_1 m_2 & l_1 n_2 & m_1 l_2 & m_1 m_2 & m_1 n_2 & n_1 l_2 & n_1 m_2 & n_1 n_2 \\ l_1 l_3 & l_1 m_3 & l_1 n_3 & m_1 l_3 & m_1 m_3 & m_1 n_3 & n_1 l_3 & n_1 m_3 & n_1 n_3 \\ l_2 l_1 & l_2 m_1 & l_2 n_1 & m_2 l_1 & m_2 m_1 & m_2 n_1 & n_2 l_1 & n_2 m_1 & n_2 n_1 \\ l_2^2 & l_2 m_2 & l_2 n_2 & m_2 l_2 & m_2^2 & m_2 n_2 & n_2 l_2 & n_2 m_2 & n_2^2 \\ l_2^0 l_3 & l_2 m_3 & l_2 n_3 & m_2 l_3 & m_2 m_3 & m_2 n_3 & n_2 l_3 & n_2 m_3 & n_2 n_3 \\ l_3 l_1 & l_3 m_1 & l_3 n_1 & m_3 l_1 & m_3 m_1 & m_3 n_1 & n_3 l_1 & n_3 m_1 & n_3 n_1 \\ l_3 l_2 & l_3 m_2 & l_3 n_2 & m_3 l_2 & m_3 m_2 & m_3 n_2 & n_3 l_2 & n_3 m_2 & n_3 n_2 \\ l_3^2 & l_3 m_3 & l_3 n_3 & m_3 l_3 & m_3^2 & m_3 n_3 & n_3 l_3 & n_3 m_3 & n_3^2 \end{bmatrix} \quad (49)$$

Since the strain increment is evaluated at the midpoint, it needs to be rotated to the midpoint configuration as

$$\Delta \boldsymbol{\varepsilon}^1 = {}^n \mathbf{Q} {}^{1/2} \mathbf{R}^T \Delta \boldsymbol{\varepsilon}^g \equiv {}^{n+(1/2)} \mathbf{Q} \Delta \boldsymbol{\varepsilon}^g \quad (50)$$

Note that the global stress at current configuration is transformed to the local stress by transformation matrix ${}^{n+1} \mathbf{Q}$ as in (47), whereas the global strain is transformed to the local strain by transformation matrix ${}^{n+(1/2)} \mathbf{Q}$. The rotation matrix ${}^{1/2} \mathbf{R}$ is approximated with half displacement as ${}^{1/2} R_{ijkl} = {}^{1/2} r_{ik} {}^{1/2} r_{jl}$ where

$${}^{1/2} r_{ij} \cong \delta_{ij} + \frac{1}{2} (\delta_{ik} - \frac{1}{4} \Delta \omega_{ik})^{-1} \Delta \omega_{kj} \quad (51)$$

Despite the fact that this approximation does not satisfy the condition $\mathbf{r} = {}^{1/2} \mathbf{r} {}^{1/2} \mathbf{r}$, the error is in second order and its material derivative is much simpler than the exact one.

In order to consider the finite deformation problem, it is necessary to obtain the updated normal vector and two tangent vectors due to the finite incremental rotation. The updated vectors are calculated as

$$\begin{aligned} {}^{n+1} \mathbf{l} &= \mathbf{r} {}^n \mathbf{l} \\ {}^{n+1} \mathbf{m} &= \mathbf{r} {}^n \mathbf{m} \\ {}^{n+1} \mathbf{n} &= \mathbf{r} {}^n \mathbf{n} \end{aligned} \quad (52)$$

3.4. Variational equation

If the structural domain at current time t_{n+1} is ${}^{n+1} \Omega$ and previous time t_n is ${}^n \Omega$, then the structural energy form at the current configuration is written as

$$a({}^{n+1} \mathbf{z}, \bar{\mathbf{z}}) = \int \int \int_{{}^{n+1} \Omega} \bar{z}_{i,n+1} x_j {}^{n+1} \sigma_{ij} \, d\Omega = \int \int \int_{{}^n \Omega} \bar{z}_{i,n} x_m F_{mj}^{-1} {}^{n+1} \sigma_{ij} J_1 \, d\Omega \quad (53)$$

where $\bar{\mathbf{z}}$ denotes the displacement variation or the virtual displacement, F_{ij} is the deformation gradient defined as $F_{ij} = \partial^{n+1} x_i / \partial^n x_j$, and $J_1 \equiv |\mathbf{F}|$ is the determinant of the deformation gradient. If a conservative force system is considered, then the external force is independent of the deformation. If we let f^B be the body force per unit volume, then the load linear form can be written as

$$\ell(\bar{\mathbf{z}}) = \int \int \int_{{}^{n+1} \Omega} \bar{z}_i f_i^B \, d\Omega = \int \int \int_{{}^n \Omega} \bar{z}_i f_i^B J_1 \, d\Omega \quad (54)$$

By equating (53) and (54), the variational equation for the nonlinear shell structure is obtained as

$$a({}^{n+1} \mathbf{z}, \bar{\mathbf{z}}) = \ell(\bar{\mathbf{z}}) \quad \text{for all } \bar{\mathbf{z}} \in Z \quad (55)$$

where

$$Z = \{ \mathbf{z} \in [H^1(\Omega)]^3 \mid \mathbf{z}(\mathbf{x}) = 0, \mathbf{x} \in \Gamma_g \} \quad (56)$$

is the space of kinematically admissible displacements, $H^1(\Omega)$ is first-order Sobolev space, and Γ_g is the essential boundary where the displacement is prescribed. The nonlinear equation

in (55) can be solved using the Newton iterative method through linearization. The linearized equation is

$$a^*({}^{n+1}\mathbf{z}^k; \Delta\mathbf{z}^{k+1}, \bar{\mathbf{z}}) = \ell(\bar{\mathbf{z}}) - a({}^{n+1}\mathbf{z}^k, \bar{\mathbf{z}}) \quad (57)$$

For a given load step, (57) is solved iteratively until the right-hand side (residual force) vanishes. The expression of $a^*({}^{n+1}\mathbf{z}^k; \Delta\mathbf{z}^{k+1}, \bar{\mathbf{z}})$ will be derived in the next section for DSA.

4. DSA OF FINITE DEFORMATION ELASTOPLASTIC SHELL STRUCTURE

Even though the adjoint variable method shows a significant efficiency for linear shell problems [12] with a large number of design variables, only the direct differentiation method is developed here because of the path-dependency of the elastoplastic problem.

4.1. Material derivative

The first step in DSA is to develop relationship between design variation and the resulting performance measure variations of the structural problem. In the DSA of shell structure, shape and configuration designs are related to the structural domain change. Therefore, it is convenient to use the material derivative in continuum mechanics to represent the structural domain variation. In order to develop first-order design sensitivity, the material point at time t_n in the perturbed domain is expressed in terms of a linear design velocity as

$${}^n\mathbf{x}_\tau = {}^n\mathbf{x} + \tau {}^n\mathbf{V} \quad (58)$$

where ${}^n\mathbf{V}(\mathbf{x})$ is the design velocity field at time t_n and τ is a scalar parameter that controls the amount of perturbation. If the structural domain changes, then the value of incremental displacement $\Delta\mathbf{z}({}^n\mathbf{x})$ also changes, in addition to its location of measurement. The point wise material derivative of incremental displacement $\Delta\mathbf{z}({}^n\mathbf{x})$ is defined as the total variation of $\Delta\mathbf{z}_\tau({}^n\mathbf{x} + \tau {}^n\mathbf{V})$ in the direction of ${}^n\mathbf{V}({}^n\mathbf{x})$, evaluated at $\tau=0$, as

$$\Delta\dot{\mathbf{z}} = \frac{d}{d\tau} \Delta\mathbf{z}_\tau({}^n\mathbf{x} + \tau {}^n\mathbf{V})|_{\tau=0} = \lim_{\tau \rightarrow 0} \left[\frac{\Delta\mathbf{z}_\tau({}^n\mathbf{x} + \tau {}^n\mathbf{V}) - \Delta\mathbf{z}({}^n\mathbf{x})}{\tau} \right] \quad (59)$$

Unlike in Section 3, the superposed dot will be used to denote the material derivative of the variable in the rest of this paper.

4.2. Design velocity in CAD geometry-based shell structure

In the updated Lagrangian formulation, the reference frame is updated after each incremental analysis using the following relation:

$${}^n\mathbf{x} = {}^0\mathbf{x} + {}^n\mathbf{z} \quad (60)$$

where ${}^n\mathbf{z}$ is the sum of the incremental displacement up to time t_n . By differentiating the above relation, the following design velocity update formula is obtained:

$$\left. \frac{d}{d\tau} ({}^n\mathbf{x}_\tau) \right|_{\tau=0} = \left. \frac{d}{d\tau} ({}^n\mathbf{x}_\tau + {}^n\mathbf{z}_\tau) \right|_{\tau=0} = {}^0\mathbf{V} + {}^n\dot{\mathbf{z}} = {}^n\mathbf{V} \quad (61)$$

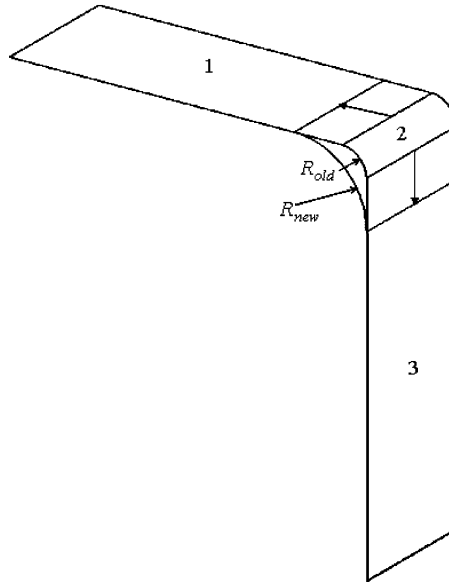


Figure 2. Design perturbation.

The computation of design velocity ${}^0\mathbf{V}$ of the undeformed configuration is directly related to the parametric representation of the neutral surface, as given in (1). For example, Figure 2 shows shell structure, which is composed of three surfaces. Each surface is characterized by its surface geometric matrix $\mathbf{G}_{i=1,2,3}$ as in (3). If the corner radius R is considered as a design parameter, the design dependence of the surface is written as

$${}^0\mathbf{x}^i(R) = \mathbf{U}(\xi)^T \mathbf{M} \mathbf{G}_i(R) \mathbf{M}^T \mathbf{W}(\eta), \quad i = 1, 2, 3 \quad (62)$$

Since geometric matrix $\mathbf{G}_i(R)$ is a function of the corner radius R , the design velocity can be obtained by perturbing R to $R + \tau \delta R$, and the differentiating with respect to τ as

$$\begin{aligned} {}^0\mathbf{V}_i &= \left. \frac{d^0\mathbf{x}_i(R + \tau \delta R)}{d\tau} \right|_{\tau=0} = \mathbf{U}(\xi)^T \mathbf{M} \left(\frac{\partial \mathbf{G}_i}{\partial R} \delta R \right) \mathbf{M}^T \mathbf{W}(\eta) \\ &= \mathbf{U}(\xi)^T \mathbf{M} (\mathbf{G}_i^{\text{new}} - \mathbf{G}_i) \mathbf{M}^T \mathbf{W}(\eta) \end{aligned} \quad (63)$$

where $\mathbf{G}_i^{\text{new}}$ is a geometric matrix of each surface when the corner radius is changed to R_{new} using the CAD geometry.

4.3. Design sensitivity analysis

A performance measure defined as

$$\psi = \iiint_{\Omega} g(\mathbf{z}, u) d\Omega \quad (64)$$

where the function g is assumed to be continuously differentiable with respect to its arguments. Differentiating the functional with respect to the design u yields

$$\psi' = \frac{d}{d\tau} \left[\int \int \int_{\Omega} g(\mathbf{z}, u) d\Omega \right] \Big|_{\tau=0} = \int \int \int_{\Omega} (g_{,z}^T \dot{\mathbf{z}} + g \operatorname{div} \mathbf{V} + g_{,u} \delta u) d\Omega \quad (65)$$

The direct differentiation method computes the first integrand on the right side of (65) by directly computing from the design sensitivity equation, which can be obtained by differentiating (55) with respect to the design variable. Since the applied load is assumed to be conservative, the differentiation of the load linear form can be carried out to obtain

$$\frac{d}{d\tau} \ell(\bar{\mathbf{z}}) \Big|_{\tau=0} = \int \int \int_{n\Omega} (\bar{z}_i f_i^B \operatorname{div} \mathbf{V}) J_1 d\Omega \equiv \ell'_V(\bar{\mathbf{z}}) \quad (66)$$

The material derivative of the structural energy form can be obtained as

$$\begin{aligned} \frac{d}{d\tau} [a^{(n+1)}(\mathbf{z}, \bar{\mathbf{z}})] \Big|_{\tau=0} &= \int \int \int_{n\Omega} [(\bar{z}_{i,n} x_m)^{\cdot} F_{mj}^{-1 n+1} \sigma_{ij}^g J_1 + \bar{z}_{i,n} x_m \dot{F}_{mj}^{-1 n+1} \sigma_{ij}^g J_1 \\ &\quad + \bar{z}_{i,n} x_m F_{mj}^{-1 n+1} \dot{\sigma}_{ij}^g J_1 + \bar{z}_{i,n} x_m F_{mj}^{-1 n+1} \sigma_{ij}^g \dot{J}_1 \\ &\quad + \bar{z}_{i,n} x_m F_{mj}^{-1 n+1} \sigma_{ij}^g \operatorname{div}^n \mathbf{V} J_1] d\Omega \end{aligned} \quad (67)$$

The material derivative terms in (67) will be investigated in the following. First, the material derivative of the gradient of the virtual displacement with respect to the position vector at the previous configuration can be found in Reference [19] as

$$(\bar{z}_{i,n} x_m)^{\cdot} = -\bar{z}_{i,n} x_k^n V_{k,n} x_m \quad (68)$$

Define $\varepsilon_{im}^V(\bar{\mathbf{z}})$ as the multiplication of the above term with the deformation gradient as

$$\varepsilon_{im}^V(\bar{\mathbf{z}}) \equiv (\bar{z}_{i,n} x_m)^{\cdot} F_{mj}^{-1} = -\bar{z}_{i,n} x_k^n V_{k,n} x_m F_{mj}^{-1} \quad (69)$$

The material derivative of the inverse of the deformation gradient and the Jacobian are obtained by exploiting well-known kinematic relations as [20]

$$\dot{F}_{mj}^{-1} = -F_{ml}^{-1} \Delta \dot{z}_{l,n+1} x_j, \quad \dot{J}_1 = J_1 \Delta \dot{z}_{k,n+1} x_k \quad (70)$$

Since the elastoplastic integration is performed with local stress, the material derivative of global stress needs to be derived from the local stress and transformation matrix as

$${}^{n+1} \dot{\boldsymbol{\sigma}}^g = {}^{n+1} \dot{\mathbf{Q}}^T {}^{n+1} \boldsymbol{\sigma}^l + {}^{n+1} \mathbf{Q}^T {}^{n+1} \dot{\boldsymbol{\sigma}}^l \quad (71)$$

The material derivative of local stress can be obtained from the constitutive relation in (39), which can be summarized as

$${}^{n+1} \boldsymbol{\sigma} = {}^n \boldsymbol{\sigma} + \mathbf{D} \Delta \boldsymbol{\varepsilon} - \Delta \lambda \mathbf{D} \mathbf{P} {}^{n+1} \boldsymbol{\eta} \quad (72)$$

and its material derivative as

$${}^{n+1} \dot{\boldsymbol{\sigma}} = {}^n \dot{\boldsymbol{\sigma}} + \mathbf{D} \Delta \dot{\boldsymbol{\varepsilon}} - \Delta \dot{\lambda} \mathbf{D} \mathbf{P} {}^{n+1} \boldsymbol{\eta} - \Delta \lambda \mathbf{D} \mathbf{P} ({}^{n+1} \dot{\boldsymbol{\sigma}} - {}^{n+1} \dot{\boldsymbol{\alpha}}) \quad (73)$$

where the elastic constitutive matrix \mathbf{D} and the mapping matrix \mathbf{P} are independent of design variables. The right side of (73) includes ${}^{n+1}\dot{\boldsymbol{\sigma}}$, which is computed at the previous time step; $\Delta\boldsymbol{\varepsilon}$, which is a function of the unknown $\dot{\mathbf{z}}$; and ${}^{n+1}\dot{\boldsymbol{\alpha}}$ and $\Delta\dot{\lambda}$, which are to be obtained from shell elastoplastic equations.

The material derivative of back stress can be obtained from the second equation in (39) as

$${}^{n+1}\dot{\boldsymbol{\alpha}} = \frac{1}{f_1} {}^n\dot{\boldsymbol{\alpha}} + \frac{f_1'}{f_1} (\Delta\dot{\lambda} {}^{n+1}\boldsymbol{\eta} + \Delta\lambda {}^{n+1}\dot{\boldsymbol{\sigma}}) \tag{74}$$

where $f_1 = 1 + \frac{2}{3}\Delta\lambda H(1-\beta)$ and $f_1' = \frac{2}{3}H(1-\beta)$. The material derivative of plastic consistency parameter $\Delta\lambda$ can be obtained from the consistency condition in (40) as

$$\Delta\dot{\lambda} = \frac{(1 - \frac{2}{3}\beta H \Delta\lambda)}{\frac{2}{3}H {}^{n+1}\phi^2} [{}^{n+1}\boldsymbol{\eta}^T \mathbf{P} {}^{n+1}\dot{\boldsymbol{\sigma}} - {}^{n+1}\boldsymbol{\eta}^T \mathbf{P} {}^n\dot{\boldsymbol{\alpha}}] - \frac{\sqrt{\frac{3}{2}}\beta f_1}{{}^{n+1}\phi} {}^n\dot{\epsilon}^p \tag{75}$$

Inserting (74) and (75) into (73) and defining $f_2 = \frac{2}{3}H {}^{n+1}\phi^2 + (1 - \frac{2}{3}\beta H \Delta\lambda) {}^{n+1}\boldsymbol{\eta}^T \mathbf{P} \boldsymbol{\Xi} \mathbf{D} \mathbf{P} {}^{n+1}\boldsymbol{\eta}$, $f_3 = f_1(1 - \frac{2}{3}\beta H \Delta\lambda)/f_2$, and $\boldsymbol{\Xi} = [f_1 \mathbf{I} + \Delta\lambda \mathbf{D} \mathbf{P}]^{-1}$, yields the final expression for the material derivative of the local stress as

$${}^{n+1}\dot{\boldsymbol{\sigma}} = \mathbf{D}^{ep} \Delta\dot{\boldsymbol{\varepsilon}} + \boldsymbol{\sigma}^{fic-1} \tag{76}$$

where

$$\mathbf{D}^{ep} = \begin{cases} \mathbf{D} & \text{(elastic)} \\ f_1 \boldsymbol{\Xi} \mathbf{D} - f_3 \boldsymbol{\Xi} \mathbf{D} \mathbf{P} {}^{n+1}\boldsymbol{\eta} {}^{n+1}\boldsymbol{\eta}^T \mathbf{P} \mathbf{D} \boldsymbol{\Xi} & \text{(plastic)} \end{cases} \tag{77}$$

$$\boldsymbol{\sigma}^{fic-1} = \begin{cases} {}^n\dot{\boldsymbol{\sigma}} & \text{(elastic)} \\ [f_1 \boldsymbol{\Xi} - f_3 \boldsymbol{\Xi} \mathbf{D} \mathbf{P} {}^{n+1}\boldsymbol{\eta} {}^{n+1}\boldsymbol{\eta}^T \mathbf{P} \boldsymbol{\Xi}] {}^n\dot{\boldsymbol{\sigma}} \\ + [\Delta\lambda \boldsymbol{\Xi} \mathbf{D} \mathbf{P} - f_3 \Delta\lambda \boldsymbol{\Xi} \mathbf{D} \mathbf{P} {}^{n+1}\boldsymbol{\eta} {}^{n+1}\boldsymbol{\eta}^T \mathbf{P} \boldsymbol{\Xi} \mathbf{D} \mathbf{P}] \\ + f_3 \Delta\lambda \boldsymbol{\Xi} \mathbf{D} \mathbf{P} {}^{n+1}\boldsymbol{\eta} {}^{n+1}\boldsymbol{\eta}^T \mathbf{P}] {}^n\dot{\boldsymbol{\alpha}} \\ + \frac{f_1 \sqrt{\frac{2}{3}}\beta H \phi}{f_2} \boldsymbol{\Xi} \mathbf{D} \mathbf{P} {}^{n+1}\boldsymbol{\eta} {}^n\dot{\epsilon}^p & \text{(plastic)} \end{cases} \tag{78}$$

For a small deformation problem, the sensitivity equation can be set up by inserting (71) and (76) into the material derivative of structural form in (67) and equating it with the material derivative of load linear form in (66) with small deformation assumptions ${}^{n+1}\mathbf{Q} = {}^n\mathbf{Q}$, $\mathbf{F} = \mathbf{I}$.

In order to extend the sensitivity equation to the finite deformation problem, material derivatives of rotation matrices in the stain increment as in (50) and in the global-to-local transformation matrix as in (48) must be considered as

$$\Delta\dot{\boldsymbol{\varepsilon}}^l = {}^n\dot{\mathbf{Q}}^{1/2} \mathbf{R}^T \Delta\boldsymbol{\varepsilon}^g + {}^n\mathbf{Q}^{1/2} \dot{\mathbf{R}}^T \Delta\boldsymbol{\varepsilon}^g + {}^n\mathbf{Q}^{1/2} \mathbf{R}^T \Delta\dot{\boldsymbol{\varepsilon}}^g \tag{79}$$

$${}^{n+1}\dot{\mathbf{Q}}^T {}^{n+1}\boldsymbol{\sigma}^l = \dot{\mathbf{R}}^n \mathbf{Q}^T {}^{n+1}\boldsymbol{\sigma}^l + \mathbf{R}^n \dot{\mathbf{Q}}^T {}^{n+1}\boldsymbol{\sigma}^l \tag{80}$$

For notational simplicity, the following relations are used:

$${}^{1/2}\dot{\mathbf{R}}^T \Delta \boldsymbol{\varepsilon}^g = \mathbf{A}^\varepsilon {}^{1/2}\dot{\mathbf{r}}, \quad \dot{\mathbf{R}} \mathbf{Q}^T {}^{n+1}\boldsymbol{\sigma}^1 = \mathbf{A}^\sigma \dot{\mathbf{r}} \quad (81)$$

where

$$\begin{aligned} A_{ijkl}^\varepsilon &= (\delta_{km} \delta_{in} r_{lj} + \delta_{im} \delta_{nj} r_{ki}) \Delta \varepsilon_{kl}^g \\ A_{ijkl}^\sigma &= (\delta_{im} \delta_{kn} r_{jl} + \delta_{jm} \delta_{nl} r_{ik}) {}^n Q_{pqkl} {}^{n+1} \sigma_{pq}^1 \end{aligned} \quad (82)$$

Taking the material derivative of (42) and (51) yields

$$\dot{\mathbf{r}} = \mathbf{B}^\sigma \Delta \dot{\boldsymbol{\omega}}, \quad {}^{1/2}\dot{\mathbf{r}} = \mathbf{B}^\varepsilon \Delta \dot{\boldsymbol{\omega}} \quad (83)$$

where

$$\begin{aligned} B_{ijkl}^\varepsilon &= (4\delta_{ik} - \Delta \omega_{ik})^{-1} (\delta_{lj} + r_{lj}) \\ B_{ijkl}^\sigma &= (2\delta_{ik} - \Delta \omega_{ik})^{-1} (\delta_{lj} + r_{lj}) \end{aligned} \quad (84)$$

The remaining steps in the procedure involve taking the material derivative of $\Delta \varepsilon_{ij}^g$ and $\Delta \omega_{ij}$ consistently with the midpoint rule. Both terms contain the material derivative of the gradient of the displacement increment with respect to the position vector at the midpoint configuration. Their material derivative thus becomes

$$(\Delta z_{i,n+1/2,x_j})' = M_{ijkl} (\Delta z_{k,n,x_p})' {}^n x_{p,n+1,x_l} = M_{ijkl} [\Delta \dot{z}_{i,n+1,x_j} + \varepsilon_{kl}^V(\Delta z)] \quad (85)$$

where

$$M_{ijkl} = {}^n x_{i,n+1/2,x_k} {}^{n+1} x_{l,n+1/2,x_j} \quad (86)$$

A detailed derivation of M_{ijkl} can be found in the literature by Fish and Shek [17]. By dividing the material derivative of $\Delta \varepsilon_{ij}^g$ and $\Delta \omega_{ij}$ into symmetric and antisymmetric parts, it can be expressed as

$$\begin{aligned} \Delta \dot{\varepsilon}_{ij} &= M_{(ij)kl} [\Delta \dot{z}_{i,n+1,x_j} + \varepsilon_{kl}^V(\Delta z)] \\ \Delta \dot{\omega}_{ij} &= M_{[ij]kl} [\Delta \dot{z}_{i,n+1,x_j} + \varepsilon_{kl}^V(\Delta z)] \end{aligned} \quad (87)$$

Define $\Delta \dot{z}_{i,n+1,x_j} \equiv \dot{v}_{i,n+1,x_j}$ for notational convenience. The final expression for the material derivative of global stress is obtained by inserting (76), (79), (80), and (87) into (71) as

$${}^{n+1}\dot{\boldsymbol{\sigma}}^g = \mathbf{C}^{\text{alg}} \dot{\mathbf{v}} + \boldsymbol{\sigma}^{\text{fic-g}} \quad (88)$$

where

$$\mathbf{C}^{\text{alg}} = [\mathbf{A}^\sigma \mathbf{B}^\sigma \hat{\mathbf{M}} + {}^{n+1} \mathbf{Q}^T \mathbf{D}^{\text{ep } n} \mathbf{Q} \mathbf{A}^\varepsilon \mathbf{B}^\varepsilon \hat{\mathbf{M}} + {}^{n+1} \mathbf{Q}^T \mathbf{D}^{\text{ep } n+1/2} \mathbf{Q} \tilde{\mathbf{M}}] \quad (89)$$

$$\boldsymbol{\sigma}^{\text{fic-g}} = \mathbf{R}^n \mathbf{Q}^T {}^{n+1} \boldsymbol{\sigma}^1 + {}^{n+1} \mathbf{Q}^T \mathbf{D}^{\text{ep } n} \dot{\mathbf{Q}}^{1/2} \mathbf{R}^T \Delta \boldsymbol{\varepsilon}^g + {}^{n+1} \mathbf{Q}^T \boldsymbol{\sigma}^{\text{fic-1}} \quad (90)$$

By using the relations in (68), (70), and (88), the material derivative of the structural energy form become

$$\left. \frac{d}{d\tau} [a^{(n+1)}(\mathbf{z}, \bar{\mathbf{z}})] \right|_{\tau=0} = a^{*(n+1)}(\mathbf{z}; \Delta\dot{\mathbf{z}}, \bar{\mathbf{z}}) + a'_V{}^{(n+1)}(\mathbf{z}, \bar{\mathbf{z}}) \quad (91)$$

where

$$a^{*(n+1)}(\mathbf{z}; \Delta\dot{\mathbf{z}}, \bar{\mathbf{z}}) = \int \int \int_{n+1\Omega} \bar{z}_{i,x_j} [C_{ijkl}^{\text{alg}} + \delta_{kl}\sigma_{ij}^{\text{g}} - \delta_{kj}\sigma_{il}] \Delta\dot{z}_{k,x_l} d\Omega \quad (92)$$

is in the same form as the linearized structural energy form in (57) if $\Delta\mathbf{z}$ is substituted into $\Delta\dot{\mathbf{z}}$. In addition,

$$a'_V{}^{(n+1)}(\mathbf{z}, \bar{\mathbf{z}}) \equiv \int \int \int_{n+1\Omega} [\varepsilon_{ij}^V(\bar{\mathbf{z}})\sigma_{ij}^{\text{g}} + \bar{z}_{i,x_j} C_{ijkl}^{\text{alg}} \varepsilon_{ij}^V(\Delta\mathbf{z}) + \bar{z}_{i,x_j} \sigma_{ij}^{\text{fic-g}} + \bar{z}_{i,x_j} \sigma_{ij}^{\text{g}} \text{div}^n \mathbf{V}] d\Omega \quad (93)$$

is the structural fictitious load form, which explicitly depends on the design velocity field ${}^n V$. After a converged solution is obtained at t_{n+1} , (93) is computed using the given design velocity field. By combining (66) and (91), the material derivative of the variational equation is obtained as

$$a^{*(n+1)}(\mathbf{z}; \Delta\dot{\mathbf{z}}, \bar{\mathbf{z}}) = \ell'_V(\bar{\mathbf{z}}) - a'_V{}^{(n+1)}(\mathbf{z}, \bar{\mathbf{z}}) \quad (94)$$

which is solved using the already decomposed tangent stiffness matrix at the converged configuration with a different fictitious load for each shape design variable. Although analysis requires an iterative method, note that the sensitivity equation in (94) is solved without iteration since $a^{*(n+1)}(\mathbf{z}; \Delta\dot{\mathbf{z}}, \bar{\mathbf{z}})$ is form-identical in nonlinear analysis.

5. MESHFREE DISCRETIZATION

Two numerical procedures are required to solve the linearized incremental equation in (57) and design sensitivity equation in (94); which are the interpolation method for the state variable and the domain integration method. The FEM approximates the state variable within an element by using piecewise polynomials. Therefore, this approximation inevitably depends on the finite element shape. In addition, since the Gauss integration method maps the finite element onto the reference element, the Jacobian matrix for the mapping depends on the finite element shape.

In the meshfree method, the state variable is approximated using a supporting set of particles in the global sense. Combined with the stabilized conforming (SC) nodal integration, the meshfree method can alleviate mesh-dependent interpolation and integration accuracy problems. Although in the initial development [21–25], the meshfree shape function is constructed from the global particle distribution, a modified approach is used in this research, such that the meshfree shape function is constructed in the parametric space Ω^f that corresponds to the neutral surface.

5.1. Meshfree method for shell structure

In the meshfree method for the shell structure, the parametric domain Ω^f of the structure is discretized by an NP number of meshfree particles. The reproducing kernel (RK) approximation

of a state variable $z(\xi, \eta)$ is [22]

$$z^R(\xi, \eta) = \sum_{I=1}^{NP} \Psi_I(\xi, \eta) \mathbf{d}_I \quad (95)$$

where \mathbf{d}_I is the approximation coefficient corresponding to the particle point (ξ_I, η_I) and Ψ_I is the meshfree shape function. Ψ_I is constructed from the smoothness requirement and the completeness condition [22]. In this paper, the cubic spline kernel function and second-order completeness condition are considered.

The shape function Ψ_I in (95) is constructed as

$$\Psi_I(\xi, \eta) = \Psi_I(\xi) = C(\xi; \xi - \xi_I) \phi_a(\xi - \xi_I) \quad (96)$$

where $\phi_a(\xi - \xi_I)$ is a kernel function that covers all meshfree particles within compact support size 'a' and $C(\xi; \xi - \xi_I)$ is a correction function [22]. For the general two-dimensional parametric domain, the kernel function in each coordinate is multiplied to obtain

$$\phi_a(\xi - \xi_I) = \phi_a(\xi - \xi_I) \phi_a(\eta - \eta_I) \quad (97)$$

Note that the nonzero region of the shape function is limited to within the compact support of the kernel function. Therefore, the summation in (95) need not be carried out over the entire NP number of meshfree particles. If IP is the number of meshfree particles that the support size covers, the summation is carried out over the IP number of meshfree particles.

The correction function in (96) is obtained from the requirement of representing a zero-, first-, and second-order polynomials exactly, and it can be constructed using a linear combination of the complete, second-order monomial bases as

$$C(\xi; \xi - \xi_I) = \mathbf{H}^T(\xi - \xi_I) \mathbf{q}(\xi) \quad (98)$$

where

$$\mathbf{H}(\xi - \xi_I) = \begin{bmatrix} 1 \\ \xi - \xi_I \\ \eta - \eta_I \\ (\xi - \xi_I)^2 \\ (\xi - \xi_I)(\eta - \eta_I) \\ (\eta - \eta_I)^2 \end{bmatrix} \quad (99)$$

is the vector of monomial bases and $\mathbf{q}(\xi) = [q_1, q_2, q_3, q_4, q_5, q_6]^T$ is the coefficient vector, which is calculated according to the reproducing condition, such that the interpolation in (96) is exact up to the second-order derivatives of function $z^R(\xi, \eta)$, which becomes a matrix

equation as

$$\mathbf{M}(\xi)\mathbf{q}(\xi) = \mathbf{H}(\mathbf{0}) \quad (100)$$

where

$$\mathbf{M}(\xi) = \sum_{I=1}^{\text{IP}} \mathbf{H}(\xi - \xi_I) \mathbf{H}^T(\xi - \xi_I) \phi_a(\xi - \xi_I) \quad (101)$$

By substituting solution $\mathbf{q}(\xi)$ from (100) into (98), the correction function $C(\xi; \xi - \xi_I)$ can be calculated, provided that $\mathbf{M}(\xi)$ is nonsingular. The compact support size 'a' has to be chosen to guarantee the positive definiteness of $\mathbf{M}(\xi)$, which is related to the order of basis function and the particle distribution density.

The RK approximation of state variable $z(\xi, \eta)$ is obtained by substituting the correction function in (98) into (96) as

$$\mathbf{z}^R(\xi, \eta) = \sum_{I=1}^{\text{IP}} \mathbf{H}^T(\mathbf{0}) \mathbf{M}^{-1}(\xi - \xi_I) \mathbf{H}(\xi - \xi_I) \phi_a(\xi - \xi_I) \mathbf{d}_I = \sum_{I=1}^{\text{IP}} \Psi_I(\xi, \eta) \mathbf{d}_I \quad (102)$$

5.2. Strain smoothing and nodal integration

The domain integration in the Galerkin meshfree methods adds considerable complexity to solution procedures. The direct nodal integration, on the other hand, leads to a numerical instability due to under-integration. A strain smoothing stabilization for the nodal integration can be used to eliminate spatial instability in the nodal integration [24]. For convergence, an integration constraint (IC) is introduced as a necessary condition for a linear exactness in the meshfree Galerkin approximation.

In order to regularize the instability due to strain localization, a strain smoothing method [24] was used in which strain is averaged over given domain using a distribution function as

$$z_{i,j}(\xi_L) = \iint_{\Omega_L} z_{i,j}(\xi) \Phi(\xi; \xi - \xi_L) \, d\Omega \quad (103)$$

where Ω_L is the nodal domain associated with particle point ξ_L as shown in Figure 3. If a following distribution function is used

$$\Phi(\xi; \xi - \xi_L) = \begin{cases} 1/A_L, & \xi \in \Omega_L \\ 0, & \xi \in \Omega_L \end{cases} \quad \text{where } A_L = \iint_{\Omega_L} \, d\Omega \quad (104)$$

then, combined with the divergence theorem, a smoothed strain becomes

$$z_{i,j}(\xi_L) = \frac{1}{A_L} \iint_{\Omega_L} z_{i,j} \, d\Omega = \frac{1}{A_L} \int_{\Gamma_L} z_i n_j \, d\Gamma \quad (105)$$

where \mathbf{n} is the outward normal vector at the boundary Γ_L . Note that the integrand has changed from the derivative of displacement into a multiplication of a displacement and a normal vector by employing the divergence theorem. In addition, Chen *et al.* [24] showed that the smoothed strain in (105) satisfies IC regardless of the numerical integration method employed.

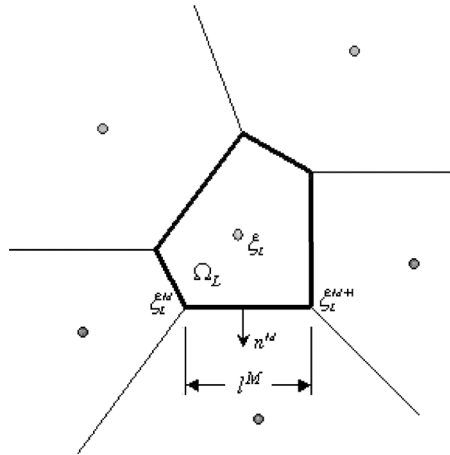


Figure 3. Geometry definition of a nodal representative domain.

If the boundary is represented by a combination of linear boundary segments, the smoothed strain in (105) can be evaluated using a two-point trapezoidal rule for each boundary segment Γ_L as

$$\begin{aligned} z_{i,j}(\xi_L) &= \frac{1}{A_L} \int_{\Gamma_L} z_i n_j \, d\Gamma = \frac{1}{A_L} \sum_{I=1}^{IP} \int_{\Gamma_L} \Psi_I d_{Ii} n_j \, d\Gamma \\ &= \frac{1}{A_L} \sum_{I=1}^{IP} \sum_{M=1}^{NS} \frac{1}{2} l^M n_j^M (\Psi_I(\xi_L^{M+1}) + \Psi_I(\xi_L^M)) d_{Ii} \equiv \sum_{I=1}^{IP} \Psi_{I,j}^{SC} d_{Ii} \end{aligned} \quad (106)$$

where l^M is the length of the M th boundary segment, and NS is the number of boundary segments. Therefore, two kinds of derivative of shape functions are calculated in advance and stored for later use: $\Psi_{I,j}^{DN}$ is calculated for the direct nodal integration at each meshfree particle from (96) as

$$\Psi_{I,j}^{DN}(\xi, \eta) \equiv \frac{\partial \Psi_I(\xi)}{\partial \xi_j} = \frac{\partial [C(\xi; \xi - \xi_I) \phi_a(\xi - \xi_I)]}{\partial \xi_j} \quad (107)$$

and $\Psi_{I,j}^{SC}$ is calculated by the smoothed conforming nodal integration as in (106).

5.3. Discretization of the shear-deformable shell structure

By using (102), the incremental displacement at a point in shell structure can be approximated using the meshfree shape function and the generalized displacement as

$$\Delta z(\xi, \eta, \zeta) = \sum_{I=1}^{IP} \Psi_I(\xi, \eta) \Delta d_I + \sum_{I=1}^{IP} \Psi_I(\xi, \eta) \frac{t_I}{2} \zeta [I_I, -m_I] \begin{bmatrix} \Delta \alpha_I \\ \Delta \beta_I \end{bmatrix} \quad (108)$$

where $\Delta \mathbf{d}_I = [\Delta d_{I1}, \Delta d_{I2}, \Delta d_{I3}]$ is the generalized displacement vector, $\Delta \alpha_I$ and $\Delta \beta_I$ are the generalized rotation vectors with respect to \mathbf{m}_I and \mathbf{l}_I , respectively, and IP is the number of particles in support. Define $\Delta \mathbf{r} \equiv [\Delta d_{I1}, \Delta d_{I2}, \Delta d_{I3}, \Delta \alpha_I, \Delta \beta_I]^T$.

The gradient of the incremental displacement with respect to the position vector is calculated using the chain rule as

$$\frac{\partial \Delta z_i}{\partial^{n+1} x_j} = \frac{\partial \Delta z_i}{\partial \xi_k} \frac{\partial \xi_k}{\partial^n x_l} \frac{\partial^n x_l}{\partial^{n+1} x_j} \quad (109)$$

where $\partial \xi_k / \partial^n x_l$ can be obtained by inverting the following relation:

$$\frac{\partial^n x_k}{\partial \xi_l} = \frac{\partial ({}^0 x_k + {}^n z_k)}{\partial \xi_l} = \frac{\partial {}^0 x_k}{\partial \xi_l} + \frac{\partial {}^n z_k}{\partial \xi_l} \quad (110)$$

where $\partial {}^0 x_k / \partial \xi_l$ is obtained from relation in (9) and $\partial {}^n z_k / \partial \xi_l$ is calculated from the ${}^n z_k$. The gradient of the incremental displacement with respect to the parametric coordinate can be obtained from (108) as

$$\frac{\partial \Delta z_i}{\partial \xi_k} = \sum_{I=1}^{\text{IP}} \mathbf{G}_I^1 \Delta \mathbf{r}_I + \zeta \sum_{I=1}^{\text{IP}} \mathbf{G}_I^2 \Delta \mathbf{r}_I \quad (111)$$

where

$$\mathbf{G}_I^1 = \begin{bmatrix} \Psi_{I,\xi}^{\text{DN}} & 0 & 0 & 0 & 0 \\ \Psi_{I,\eta}^{\text{DN}} & 0 & 0 & 0 & 0 \\ 0 & 0 & 0 & \frac{1}{2} \Psi_{ItI} l_{I1} & -\frac{1}{2} \Psi_{ItI} m_{I1} \\ 0 & \Psi_{I,\xi}^{\text{DN}} & 0 & 0 & 0 \\ 0 & \Psi_{I,\eta}^{\text{DN}} & 0 & 0 & 0 \\ 0 & 0 & 0 & \frac{1}{2} \Psi_{ItI} l_{I2} & -\frac{1}{2} \Psi_{ItI} m_{I2} \\ 0 & 0 & \Psi_{I,\xi}^{\text{DN}} & 0 & 0 \\ 0 & 0 & \Psi_{I,\eta}^{\text{DN}} & 0 & 0 \\ 0 & 0 & 0 & \frac{1}{2} \Psi_{ItI} l_{I3} & -\frac{1}{2} \Psi_{ItI} m_{I3} \end{bmatrix} \quad (112)$$

is the contribution from the membrane and transverse shear, and

$$\mathbf{G}_I^2 = \begin{bmatrix} 0 & 0 & 0 & \frac{1}{2}\Psi_{I,\xi}^{\text{SC}}t_{Il1} & -\frac{1}{2}\Psi_{I,\xi}^{\text{SC}}t_{Im1} \\ 0 & 0 & 0 & \frac{1}{2}\Psi_{I,\eta}^{\text{SC}}t_{Il1} & -\frac{1}{2}\Psi_{I,\eta}^{\text{SC}}t_{Im1} \\ 0 & 0 & 0 & 0 & 0 \\ 0 & 0 & 0 & \frac{1}{2}\Psi_{I,\xi}^{\text{SC}}t_{Il2} & -\frac{1}{2}\Psi_{I,\xi}^{\text{SC}}t_{Im2} \\ 0 & 0 & 0 & \frac{1}{2}\Psi_{I,\eta}^{\text{SC}}t_{Il2} & -\frac{1}{2}\Psi_{I,\eta}^{\text{SC}}t_{Im2} \\ 0 & 0 & 0 & 0 & 0 \\ 0 & 0 & 0 & \frac{1}{2}\Psi_{I,\xi}^{\text{SC}}t_{Il3} & -\frac{1}{2}\Psi_{I,\xi}^{\text{SC}}t_{Im3} \\ 0 & 0 & 0 & \frac{1}{2}\Psi_{I,\eta}^{\text{SC}}t_{Il3} & -\frac{1}{2}\Psi_{I,\eta}^{\text{SC}}t_{Im3} \\ 0 & 0 & 0 & 0 & 0 \end{bmatrix} \quad (113)$$

is the contribution from the bending.

It is well known that when a full integration is used to evaluate the membrane–shear part, the numerical solution exhibits shear and membrane locking. Therefore, two kinds of derivative of the meshfree shape function are calculated using (106) and (107): one is constructed based on the direct nodal integration for the membrane and transverse shear, $\Psi_{I,\xi}^{\text{DN}}$ and $\Psi_{I,\eta}^{\text{DN}}$, as in (112); and the other is constructed based on the SC nodal integration for the bending, $\Psi_{I,\xi}^{\text{SC}}$ and $\Psi_{I,\eta}^{\text{SC}}$, as in (113). The gradient of the incremental displacement with respect to the position vector in (109) can be obtained using above equations as

$$\begin{bmatrix} \frac{\partial \Delta z_i}{\partial^n x_j} \end{bmatrix}_{9 \times 1} = \sum_{I=1}^{\text{IP}} \mathbf{T} \mathbf{G}_I^1 \Delta \mathbf{r}_I + \zeta \sum_{I=1}^{\text{IP}} \mathbf{T} \mathbf{G}_I^2 \Delta \mathbf{r}_I \equiv \sum_{I=1}^{\text{IP}} \mathbf{B}_I \Delta \mathbf{r}_I \quad (114)$$

where

$$\mathbf{T} \equiv \begin{bmatrix} \mathbf{J}^{-1} & \mathbf{0} & \mathbf{0} \\ \mathbf{0} & \mathbf{J}^{-1} & \mathbf{0} \\ \mathbf{0} & \mathbf{0} & \mathbf{J}^{-1} \end{bmatrix}_{9 \times 9} \quad (115)$$

and

$$\mathbf{J}^{-1} = \begin{bmatrix} \frac{\partial \xi_i}{\partial^n x_j} \end{bmatrix}_{3 \times 3} \quad (116)$$

Then the local strain vector is calculated by using the gradient of incremental displacement with respect to the position vector in (114) as

$$\boldsymbol{\varepsilon}(\Delta \mathbf{z}) = \begin{bmatrix} \frac{\partial \Delta z_i}{\partial^{n+1} x_j} \end{bmatrix}_{9 \times 1} = \sum_{I=1}^{\text{IP}} \mathbf{L} \mathbf{B}_I \Delta \mathbf{r}_I \quad (117)$$

where

$$\mathbf{L} \equiv \begin{bmatrix} \mathbf{F}^{-1} & \mathbf{0} & \mathbf{0} \\ \mathbf{0} & \mathbf{F}^{-1} & \mathbf{0} \\ \mathbf{0} & \mathbf{0} & \mathbf{F}^{-1} \end{bmatrix} \quad (118)$$

and

$$\mathbf{F}^{-1} = \begin{bmatrix} \frac{\partial^n x_i}{\partial^{n+1} x_j} \end{bmatrix}_{3 \times 3} \quad (119)$$

Discretization of the linearized variational form $a^*(n+1, \mathbf{z}^k; \Delta \mathbf{z}^{k+1}, \bar{\mathbf{z}})$ in (57) becomes

$$\sum_{p=1}^{\text{NP}} \int_R \left\{ \sum_{I=1}^{\text{IP}} \sum_{J=1}^{\text{IP}} \bar{\mathbf{r}}_I^T \mathbf{B}_I^T \mathbf{L}^T \mathbf{C}^{\text{eff}} \mathbf{L} \mathbf{B}_J \Delta \mathbf{r}_J \right\} J_1 |\mathbf{J}| d\zeta A_p \equiv \hat{\bar{\mathbf{r}}}^T \mathbf{K}_s \Delta \hat{\mathbf{r}} \quad (120)$$

where $\hat{\bar{\mathbf{r}}}$ and $\Delta \hat{\mathbf{r}}$ denote the global displacement and rotation vectors, \mathbf{K}_s is the global stiffness matrix, A_p is the area of a meshfree particle representative domain, ζ is the parametric coordinate in thickness direction, and

$$[\mathbf{C}^{\text{eff}}]_{9 \times 9} = \mathbf{C}^{\text{eff}} \equiv C_{ijkl}^{\text{alg}} + \delta_{kl} \sigma_{ij}^g - \delta_{kj} \sigma_{il} \quad (121)$$

as shown in (92). In (120), J_1 represents the Jacobian between configuration at time t_n and t_{n+1} and $|\mathbf{J}|$ represents the Jacobian between the parametric coordinate and physical coordinate at time t_n . The right side of (57) can be defined as the residual force vectors, which are discretized as

$$\hat{\bar{\mathbf{z}}}^T \mathbf{F}^{\text{ext}} = \sum_{p=1}^{\text{NP}} \int_R \bar{\mathbf{z}}^T \mathbf{f}^B J_1 |\mathbf{J}| d\zeta A_p \quad (122)$$

for $\ell(\bar{\mathbf{z}})$ and

$$\hat{\bar{\mathbf{r}}}^T \mathbf{F}^{\text{int}} = \sum_{p=1}^{\text{NP}} \int_R \sum_{I=1}^{\text{IP}} \bar{\mathbf{r}}_I^T \mathbf{B}_I^T \mathbf{L}^T \boldsymbol{\sigma} J_1 |\mathbf{J}| d\zeta A_p \quad (123)$$

for $a(n+1, \mathbf{z}^k, \bar{\mathbf{z}})$. Thus, the discretized global matrix equation is, from (120), (122), and (123),

$$\hat{\bar{\mathbf{r}}}^T \mathbf{K}_s \Delta \hat{\mathbf{r}} = \hat{\bar{\mathbf{z}}}^T \mathbf{F}^{\text{ext}} - \hat{\bar{\mathbf{r}}}^T \mathbf{F}^{\text{int}} \quad (124)$$

Since the space of kinematically admissible displacement cannot be chosen easily from the generalized displacement, the variation of the generalized displacement and rotation should be transformed to the variation of the physical displacement and rotation. From (108), the displacement at the neutral surface is

$$\Delta \mathbf{z}_J = \Delta \mathbf{z}(\zeta_J, \eta_J) = \sum_{I=1}^{\text{IP}} \Psi_I(\zeta_J, \eta_J) \Delta \mathbf{d}_I \quad (125)$$

Equation (125) can be extended to include the generalized rotation as

$$\begin{bmatrix} \Delta z_J \\ \Delta z_{4J} \\ \Delta z_{5J} \end{bmatrix} = \begin{bmatrix} \Delta z(\xi_J, \eta_J) \\ \Delta z_4(\xi_J, \eta_J) \\ \Delta z_5(\xi_J, \eta_J) \end{bmatrix} = \sum_{I=1}^{\text{IP}} \Psi_I(\xi_J, \eta_J) \Delta \mathbf{r}_I \equiv \sum_{I=1}^{\text{IP}} A_{IJ} \Delta \mathbf{r}_I \quad (126)$$

where Δz_4 and Δz_5 are the physical rotational increments. Thus, the relation between the physical and the generalized displacement and rotation can be obtained as

$$\hat{\mathbf{z}} = \mathbf{A}^T \hat{\mathbf{r}} \quad (127)$$

where \mathbf{A} is the transformation matrix. By using the relation in (127), the variation of the generalized displacement in (124) is transformed to the variation of the physical displacement as

$$\hat{\mathbf{z}}^T \mathbf{A}^{-1} \mathbf{K}_S \Delta \hat{\mathbf{r}} = \hat{\mathbf{z}}^T \mathbf{F}^{\text{ext}} - \hat{\mathbf{z}}^T \mathbf{A}^{-1} \mathbf{F}^{\text{int}} \quad (128)$$

Thus, the final governing matrix equation is

$$\mathbf{A}^{-1} \mathbf{K}_S \Delta \hat{\mathbf{r}} = \mathbf{F}^{\text{ext}} - \mathbf{A}^{-1} \mathbf{F}^{\text{int}} \quad (129)$$

which can be solved for the solution.

5.4. Meshfree discretization of design sensitivity equation

To numerically compute the design sensitivity coefficient, the design sensitivity equation in (94) is discretized following the same procedure as the response analysis. For this purpose, it is necessary to discretize $a'_V(n+1, \bar{\mathbf{z}})$ and $\ell'_V(\bar{\mathbf{z}})$ consistently with the method presented in Section 5.3.

In the solid structure, meshfree shape function Ψ_I is constructed on physical domain Ω , whose shape is a design variable. Thus, Ψ_I is a function of the design variable. However, in the shell structure, the Ψ_I is independent of the design because it is calculated on a parametric domain Ω' and the design dependence is established through the Jacobian matrix between parametric coordinate and physical coordinate. Even though Ψ_I is independent of the design, the displacement approximation in (108) has explicitly dependent terms on the design through unit vectors \mathbf{l}_I and \mathbf{m}_I . The explicit dependence (implicit dependence is taken care by the term on the left of (94)) can be represented as

$$\Delta \mathbf{z}^{\text{fic}} = \sum_{I=1}^{\text{IP}} \Psi_I(\xi, \eta) \frac{l_I}{2} \zeta [\dot{\mathbf{l}}_I, -\dot{\mathbf{m}}_I] \begin{bmatrix} \Delta \alpha_I \\ \Delta \beta_I \end{bmatrix} \quad (130)$$

Then, $\boldsymbol{\varepsilon}^V(\Delta \mathbf{z})$ in (87) can be discretized by using (130) as

$$\begin{aligned} \boldsymbol{\varepsilon}^V(\Delta \mathbf{z}) &= \sum_{I=1}^{\text{IP}} \mathbf{L} \mathbf{T}_V \mathbf{G}_I^1 \Delta \mathbf{r}_I + \sum_{I=1}^{\text{IP}} \mathbf{L} \mathbf{T} \mathbf{G}_{V_I}^1 \Delta \mathbf{r}_I + \sum_{I=1}^{\text{IP}} \mathbf{L} \mathbf{T}_V \mathbf{G}_I^2 \Delta \mathbf{r}_I + \sum_{I=1}^{\text{IP}} \mathbf{L} \mathbf{T} \mathbf{G}_{V_I}^2 \Delta \mathbf{r}_I \\ &\equiv \sum_{I=1}^{\text{IP}} \mathbf{L} \mathbf{B}_I^V \Delta \mathbf{r}_I \end{aligned} \quad (131)$$

where

$$\mathbf{G}_{VI}^1 = \begin{bmatrix} 0 & 0 & 0 & 0 & 0 \\ 0 & 0 & 0 & 0 & 0 \\ 0 & 0 & 0 & \frac{1}{2}\Psi_{I,t_I}\dot{l}_{I1} & -\frac{1}{2}\Psi_{I,t_I}\dot{m}_{I1} \\ 0 & 0 & 0 & 0 & 0 \\ 0 & 0 & 0 & 0 & 0 \\ 0 & 0 & 0 & \frac{1}{2}\Psi_{I,t_I}\dot{l}_{I2} & -\frac{1}{2}\Psi_{I,t_I}\dot{m}_{I2} \\ 0 & 0 & 0 & 0 & 0 \\ 0 & 0 & 0 & 0 & 0 \\ 0 & 0 & 0 & \frac{1}{2}\Psi_{I,t_I}\dot{l}_{I3} & -\frac{1}{2}\Psi_{I,t_I}\dot{m}_{I3} \end{bmatrix} \quad (132)$$

$$\mathbf{G}_{VI}^2 = \begin{bmatrix} 0 & 0 & 0 & \frac{1}{2}\Psi_{I,\xi}^{\text{sc}}t_I\dot{l}_{I1} & -\frac{1}{2}\Psi_{I,\xi}^{\text{sc}}t_I\dot{m}_{I1} \\ 0 & 0 & 0 & \frac{1}{2}\Psi_{I,\eta}^{\text{sc}}t_I\dot{l}_{I1} & -\frac{1}{2}\Psi_{I,\eta}^{\text{sc}}t_I\dot{m}_{I1} \\ 0 & 0 & 0 & 0 & 0 \\ 0 & 0 & 0 & \frac{1}{2}\Psi_{I,\xi}^{\text{sc}}t_I\dot{l}_{I2} & -\frac{1}{2}\Psi_{I,\xi}^{\text{sc}}t_I\dot{m}_{I2} \\ 0 & 0 & 0 & \frac{1}{2}\Psi_{I,\eta}^{\text{sc}}t_I\dot{l}_{I2} & -\frac{1}{2}\Psi_{I,\eta}^{\text{sc}}t_I\dot{m}_{I2} \\ 0 & 0 & 0 & 0 & 0 \\ 0 & 0 & 0 & \frac{1}{2}\Psi_{I,\xi}^{\text{sc}}t_I\dot{l}_{I3} & -\frac{1}{2}\Psi_{I,\xi}^{\text{sc}}t_I\dot{m}_{I3} \\ 0 & 0 & 0 & \frac{1}{2}\Psi_{I,\eta}^{\text{sc}}t_I\dot{l}_{I3} & -\frac{1}{2}\Psi_{I,\eta}^{\text{sc}}t_I\dot{m}_{I3} \\ 0 & 0 & 0 & 0 & 0 \end{bmatrix} \quad (133)$$

$$\mathbf{T}_V = \begin{bmatrix} \mathbf{J}_0^{-1} \frac{\partial \mathbf{V}}{\partial \mathbf{x}} & \mathbf{0} & \mathbf{0} \\ \mathbf{0} & \mathbf{J}_0^{-1} \frac{\partial \mathbf{V}}{\partial \mathbf{x}} & \mathbf{0} \\ \mathbf{0} & \mathbf{0} & \mathbf{J}_0^{-1} \frac{\partial \mathbf{V}}{\partial \mathbf{x}} \end{bmatrix} \quad (134)$$

and $\Psi_{I,j}^{SC}$ is calculated by the smoothed conforming nodal integration as in (106). The global structural fictitious load form, $a'_V(n+1, \bar{\mathbf{z}}, \bar{\mathbf{z}})$, in (93) can be discretized as

$$\begin{aligned} & \hat{\mathbf{r}}^T \mathbf{F}_S^{\text{fic}} \\ &= \sum_{p=1}^{\text{NP}} \int_R \left\{ \sum_{I=1}^{\text{IP}} \sum_{J=1}^{\text{IP}} \bar{\mathbf{r}}_I^T [\mathbf{B}_I^T \mathbf{L}^T \mathbf{C}^{\text{eff}} \mathbf{L}^T \mathbf{B}_J^V] \Delta \mathbf{r}_J \right\} J_1 |J_0| d\zeta A_p \\ &+ \sum_{p=1}^{\text{NP}} \int_R \left\{ \sum_{I=1}^{\text{IP}} \bar{\mathbf{r}}_I^T [\mathbf{B}_I^V \mathbf{L}^T \mathbf{n}^{n+1} \boldsymbol{\sigma}^g + \mathbf{B}_I^T \mathbf{L}^T \mathbf{n}^{n+1} \boldsymbol{\sigma}^{\text{fic-g}} + \mathbf{B}_I^T \mathbf{L}^T \mathbf{n}^{n+1} \boldsymbol{\sigma}^g \text{div}^n \mathbf{V}] \right\} \\ &\times J_1 |J_0| d\zeta A_p \end{aligned} \tag{135}$$

where $\mathbf{n}^{n+1} \boldsymbol{\sigma}^g$ is the stress at current configuration. The external fictitious load form, $\ell'_V(\bar{\mathbf{z}})$, in (66) can be discretized as

$$\hat{\bar{\mathbf{z}}}^T \mathbf{F}_\ell^{\text{fic}} = \sum_{p=1}^{\text{NP}} \int_R \bar{\mathbf{z}}^T \mathbf{f}^B \text{div}^n \mathbf{V} J_1 |J_0| d\zeta A_p \tag{136}$$

Then the global design sensitivity equation is

$$\hat{\mathbf{r}}^T \mathbf{K}_S \Delta \hat{\mathbf{r}} = \hat{\bar{\mathbf{z}}}^T \mathbf{F}_\ell^{\text{fic}} - \hat{\mathbf{r}}^T \mathbf{F}_S^{\text{fic}} \tag{137}$$

Pre-multiplying \mathbf{A}^{-1} to (137) as in the response analysis in (128), yields the discretized sensitivity equation as

$$\hat{\bar{\mathbf{z}}}^T \mathbf{A}^{-1} \mathbf{K}_S \Delta \hat{\mathbf{r}} = \hat{\bar{\mathbf{z}}}^T \mathbf{F}_\ell^{\text{fic}} - \hat{\bar{\mathbf{z}}}^T \mathbf{A}^{-1} \mathbf{F}_S^{\text{fic}} \tag{138}$$

Therefore, the final equation is

$$\mathbf{A}^{-1} \mathbf{K}_S \Delta \hat{\mathbf{r}} = \mathbf{F}_\ell^{\text{fic}} - \mathbf{A}^{-1} \mathbf{F}_S^{\text{fic}} \tag{139}$$

The left side of (139) is same form as in (129). Thus, the same stiffness matrix that is already decomposed is used to solve sensitivity equation. This makes the design sensitivity calculation very efficient.

6. NUMERICAL EXAMPLES

In order to demonstrate accuracy and efficiency of the proposed continuum-based DSA method of nonlinear shell structure and its application to design optimization, two example problems are provided in this section.

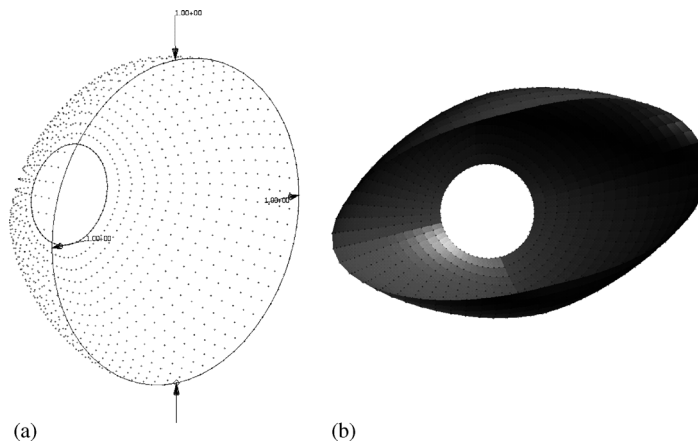


Figure 4. Pinched hemisphere: (a) meshfree discretization; and (b) displacement.

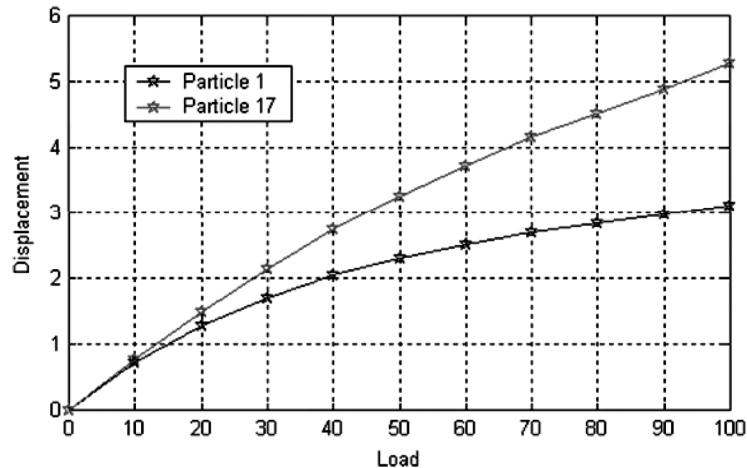


Figure 5. Load–displacement curve of the pinched hemisphere.

6.1. DSA of pinched hemisphere

A pinched hemispherical shell with an 18° hole at the top, under two inward and two outward forces 90° apart, as shown in Figure 4, is a frequent example for discussing shell structures [26, 27]. Because of symmetry conditions, only one quadrant is modelled.

The material properties of this problem are Young's modulus, $E = 6.825 \times 10^7$, Poisson's ratio $\nu = 0.3$, radius $R = 10$, and thickness $t = 0.04$. The yield stress is $\sigma_Y = 2.43 \times 10^5$ and the hardening slope is $H = 3.0 \times 10^5$. A total of 289 meshfree particles are distributed in the quadrant of the structure, which corresponds to 1445 degrees-of-freedom. Fourteen time steps have been used to complete the nonlinear analysis. Seven integration points are used through the thickness direction. It took 5720 s for response on J-class HP workstation. Figure 5 shows

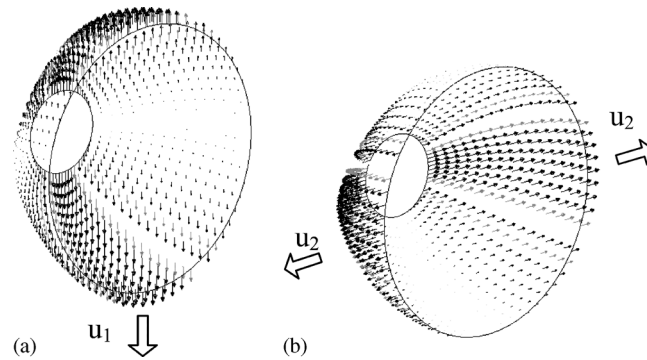


Figure 6. Design velocity fields: (a) u_1 ; and (b) u_2 .

Table I. Accuracy of design sensitivity results.

Design variable	Performance measure	$\Delta\psi$	$\psi' \times \Delta\tau$	$(\Delta\psi/\psi' \Delta\tau) \times 100$
u_1	Z_1	3.8048E-3	3.8058E-3	99.97
	Z_{17}	-7.5058E-3	-7.5033E-3	100.03
	Z_{96}	5.2653E-4	5.2648E-4	100.01
	Z_{164}	4.3113E-4	4.3072E-4	100.10
	Z_{175}	-6.5461E-5	-6.5408E-5	100.08
	Z_{199}	3.4780E-4	3.4844E-4	99.82
u_2	Z_1	-1.3431E-3	-1.3427E-3	100.03
	Z_{17}	1.6425E-3	1.6426E-3	100.00
	Z_{96}	2.9782E-4	2.9778E-4	100.01
	Z_{164}	-4.7477E-5	-4.7482E-5	99.99
	Z_{175}	5.0661E-5	5.0696E-5	99.93
	Z_{199}	-1.5235E-5	-1.5336E-5	99.34

load–displacement curve at two points where forces are applied. As it can be seen from the figure, nonlinear behaviour is well captured.

DSA is carried out using the design velocity fields shown in Figure 6 indicated by arrows. The computational cost of DSA per design parameter is 177 s, which is about 3.1% of the response analysis cost, which is very efficient compared to the FDM.

The design sensitivity results are shown in Table I. The first column denotes the design variable ID; the second column denotes the performance measure, which is the vertical displacement; the third column denotes is the finite difference result $\Delta\psi$ with perturbation size $\Delta\tau = 10^{-2}$, the fourth column denotes first-order approximation $\psi' \times \Delta\tau$ using the proposed sensitivity results, and the last column compares the results between the third and fourth columns. Very accurate sensitivity results are obtained, as shown is Table I.

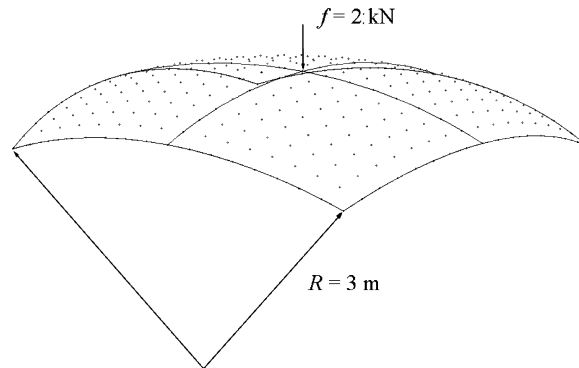


Figure 7. Meshfree discretization of a spherical shell structure.

Table II. Material properties.

Properties	Value
Young's modulus, E	70 GPa
Poisson's ratio, ν	0.35135
Yielding strength, σ_Y	241 MPa
Hardening slope, H	241 MPa

6.2. Optimization of a spherical shell structure

In this section, a spherical shell structure is used in order to demonstrate use of the proposed design sensitivity method for design optimization. The shell structure illustrated in Figure 7 is modelled using a single spline surface obtained using the MSC/PATRAN geometric modeller. Three translational degrees-of-freedom are fixed along the edge of the structure, and a vertical load of 2000 N is applied at the centre. A total of 289 meshfree particles are distributed on the surface, which corresponds to 1445 degrees-of-freedom. Table II shows the material properties of the structure. A constant thickness $t = 1$ mm is used.

Meshfree nonlinear analysis is carried out using the incremental procedure. The size of the dilation parameter is determined such that every point covers five particle points in each spatial direction. Domain integration is carried out at each particle point using the stabilized-conforming (SC) nodal integration method. As with the linear shell formulation, the direct nodal integration is employed to remove the membrane and shear locking phenomena. Refer to Reference [12] for the linear shell formulation. The values of the residual norm during the typical Newton–Raphson iteration are shown in Table III. This result clearly exhibits a quadratic convergence of meshfree analysis.

For meshfree analysis, the numerical integration must be carried out through the thickness direction. In this example, the seven-point Gauss integration method is employed through the thickness direction. Figure 8 shows the von Mises stresses result from meshfree analysis. Due

Table III. Residual norm of the elastoplastic analysis.

Iteration	Residual norm
1	6.50061E + 02
2	7.41409E + 01
3	1.82775E - 01
4	4.26552E - 07

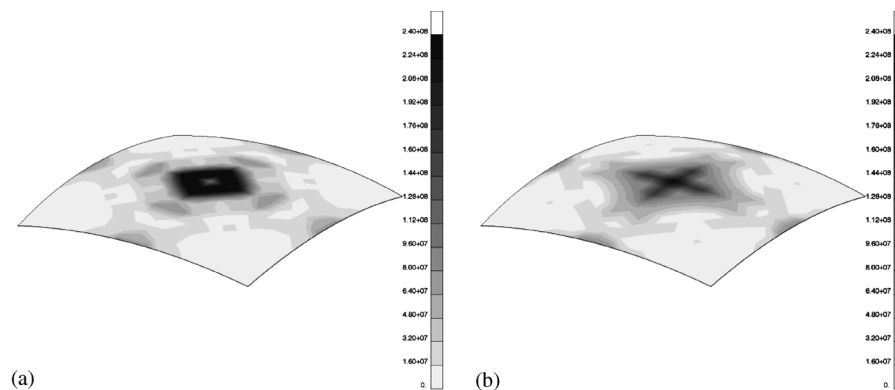


Figure 8. von Mises stresses of the spherical shell structure: (a) top; and (b) bottom.

to the concentrated load, large stress appears at the centre of the structure. Figure 8(a) shows the von Mises stresses at the first integration point, which is close to the top surface; while Figure 8(b) shows the stresses at the last integration point, which is close to the bottom surfaces. Due to the bending contribution, stresses of the shell structure have different values at the top and bottom surfaces.

The shape and configuration DSA is carried out by using six design parameters, which are illustrated in Figure 9. The first design parameter is x component of the tangent vector \mathbf{p}^ξ in ξ direction at four corner points as shown in Figure 9(a). Similarly, the second and the third design parameters are x, y, z component of the tangent vector \mathbf{p}^η in η direction at four corner points. Using these design parameters, the corresponding design velocity field is calculated in the parametric space.

The accuracy of the proposed DSA is compared with the FDM in Table IV. The first column denotes the design variable ids; the second column denotes various performance measures such as volume, vertical displacement, stress, von Mises stress, and effective plastic strain (the superscript ' u ' and ' b ' are used to denote measures at top and bottom surface, respectively); the third column denotes the performance values at the initial design; the fourth column denotes the perturbed results from FDM; the fifth column denotes the prediction from the calculated sensitivity results; and the last column compares the results between the fourth and fifth columns. Very accurate sensitivity results are obtained, as shown throughout Table IV. A small perturbation of $\tau = 10^{-3}$ is used for FDM.

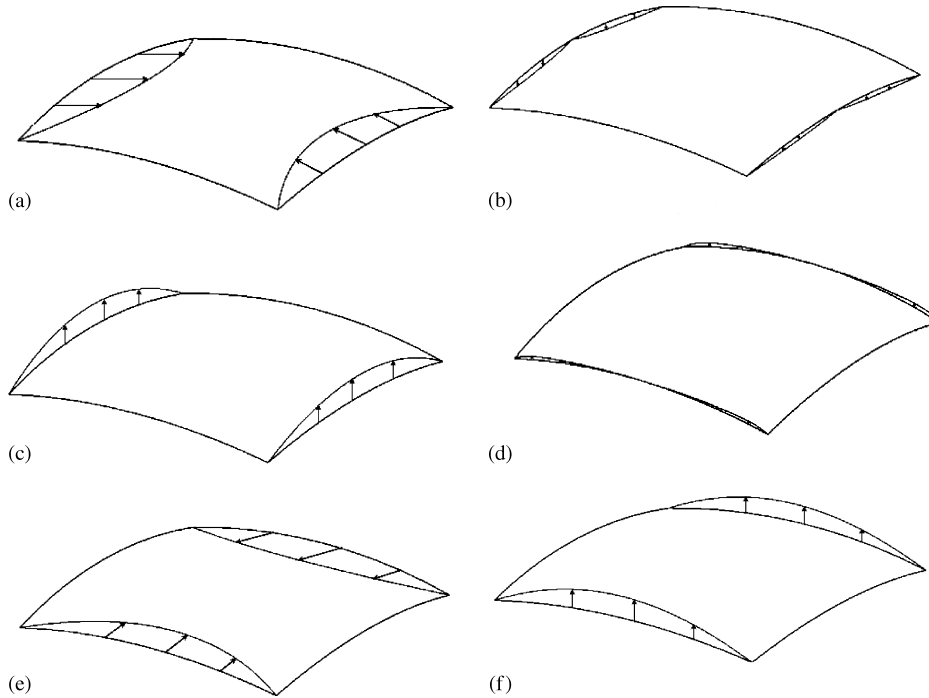


Figure 9. Design parameterization of the spherical shell structure:
(a) u_1 ; (b) u_2 ; (c) u_3 ; (d) u_4 ; (e) u_5 ; and (f) u_6 .

The design optimization problem is formulated as in (140) where the values in the parenthesis are the performance values at the initial design.

$$\begin{aligned}
 & \min \quad \text{Volume} \\
 & \text{s.t.} \quad \sigma_{vM145}^u(113.05) \leq 113.05 \text{ MPa} \\
 & \quad \quad \bar{e}_{145}^{p^b}(1.47 \times 10^{-2}) \leq 1.00 \times 10^{-4}
 \end{aligned} \tag{140}$$

The volume of the spherical shell structure is to be minimized with constraints on the effective plastic strain and von Mises stress at the point where the concentrated force is applied because the point has maximum deformation and thus maximum stress. The initial design is infeasible since one constraint is violated. Figure 10 shows the history of the cost and constraint functions. As shown in Figure 10, the most volume reduction is achieved in first three iterations even though the initial design was an infeasible one. The optimum solution is obtained after 10 iterations and all the constraints are satisfied. The constraint violations are adjusted during the last three iterations. The cost function, which is the volume of the structure, is reduced up to 29.1% of the initial design. The von Mises stress is decreased up to 58.5% of the initial design and the effective plastic strain is decreased significantly to become almost zero as shown in

Table IV. Accuracy of the sensitivity analysis results.

Design variable	Performance measure	ψ	$\Delta\psi$	$\psi' \times \Delta\tau$	$(\Delta\psi/\psi' \times \Delta\tau) \times 100$
1	Volume	1.05682E - 03	3.39312E - 10	3.39312E - 10	100.00
	Z_{23}	-4.83115E - 05	-2.21692E - 10	-2.21690E - 10	100.00
	σ_{1154}^u	3.62922E + 06	-7.78925E + 00	-7.78937E + 00	100.00
	σ_{vM145}^u	1.13045E + 08	2.63158E + 01	2.63149E + 01	100.00
	Z_{175}	3.21838E - 04	5.19739E - 10	5.19742E - 10	100.00
	σ_{22199}^b	5.13991E + 06	8.55478E + 00	8.55491E + 00	100.00
	e_{145}^b	1.47175E - 02	3.68249E - 10	3.68238E - 10	100.00
	3	Volume	1.05682E - 03	7.92338E - 11	7.92332E - 11
Z_{23}		-4.83115E - 05	2.78742E - 10	2.78741E - 10	100.00
σ_{1154}^u		3.62922E + 06	3.59937E + 00	3.59930E + 00	100.00
σ_{vM145}^u		1.13045E + 08	2.59240E + 01	2.59246E + 01	100.00
Z_{175}		3.21838E - 04	1.76443E - 09	1.76444E - 09	100.00
σ_{22199}^b		5.13991E + 06	1.20911E + 01	1.20910E + 01	100.00
e_{145}^b		1.47175E - 02	-8.32310E - 08	-8.32313E - 08	100.00
4		Volume	1.05682E - 03	-3.72615E - 12	-3.72655E - 12
	Z_{23}	-4.83115E - 05	3.13598E - 10	3.13600E - 10	100.00
	σ_{1154}^u	3.62922E + 06	2.15412E + 00	2.15393E + 00	100.01
	σ_{vM145}^u	1.13045E + 08	2.60905E + 01	2.60906E + 01	100.00
	Z_{175}	3.21838E - 04	-2.46418E - 10	-2.46408E - 10	100.00
	σ_{22199}^b	5.13991E + 06	-4.41299E + 00	-4.41287E + 00	100.00
	e_{145}^b	1.47175E - 02	1.89659E - 09	1.89659E - 09	100.00
	6	Volume	1.05682E - 03	7.92338E - 11	7.92332E - 11
Z_{23}		-4.83115E - 05	8.31410E - 10	8.31424E - 10	100.00
σ_{1154}^u		3.62922E + 06	-1.44313E + 00	-1.44300E + 00	100.01
σ_{vM145}^u		1.13045E + 08	2.59233E + 01	2.59245E + 01	100.00
Z_{175}		3.21838E - 04	-2.87507E - 09	-2.87509E - 09	100.00
σ_{22199}^b		5.13991E + 06	-5.75857E + 01	-5.75861E + 01	100.00
e_{145}^b		1.47175E - 02	-8.32310E - 08	-8.32313E - 08	100.00

Figure 10. Figure 11 shows the design parameter history. Since the shape design parameters are set to zero at the initial design, all the design parameters start from the origin of the graph shown in Figure 11.

The optimum shape is obtained with decreased radius R as shown in Figure 12. Therefore, some amount of the bending deformation in the initial design is turned into membrane deformation in optimized design. Figure 13 shows the von Mises stress results of the optimized design. Compared with the results of the initial design, it can be noticed that the stresses are significantly decreased despite the reduced volume.

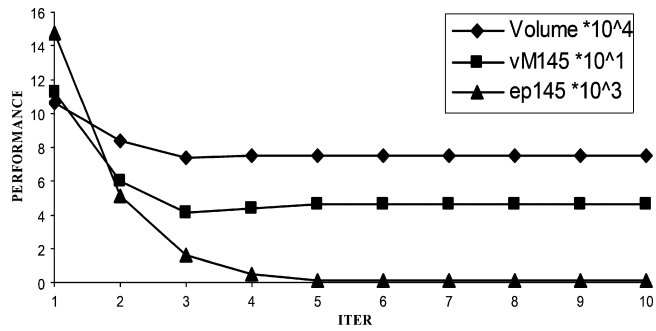


Figure 10. Optimization history of spherical shell structure.

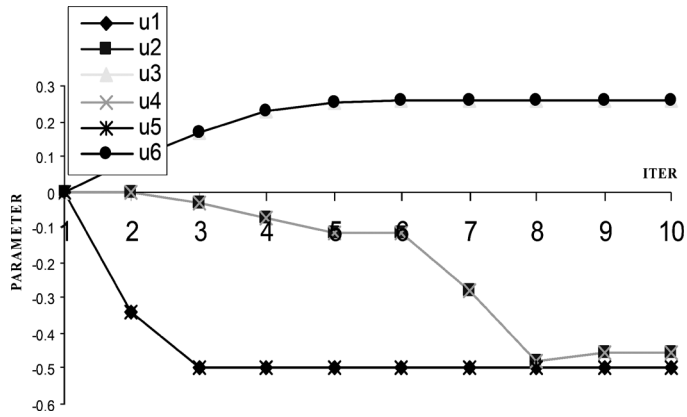


Figure 11. Design parameter history of spherical shell structure.

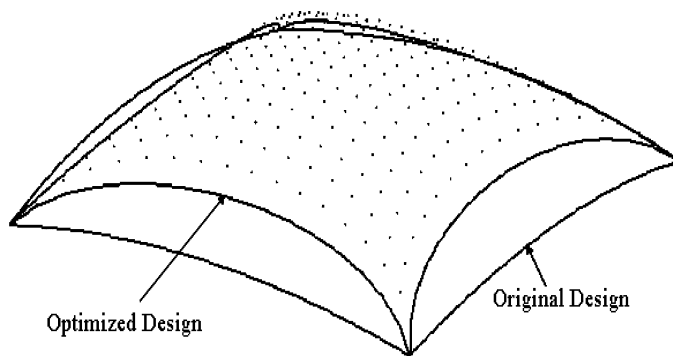


Figure 12. Optimum design of spherical shell structure.

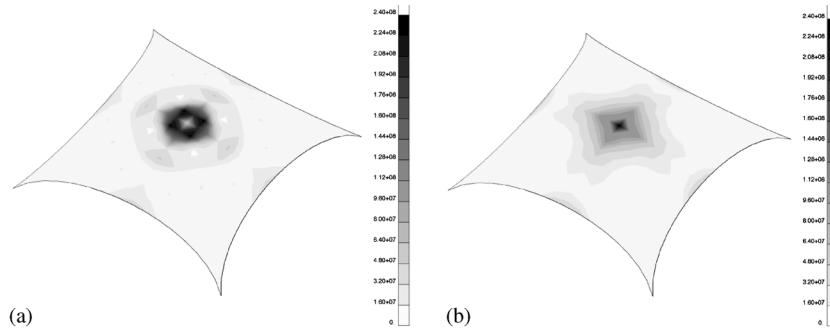


Figure 13. von Mises stresses of the optimized spherical shell structure: (a) top; and (b) bottom.

7. CONCLUSION

A continuum-based DSA method for the finite deformation elastoplastic shell structure has been proposed. Shell elastoplasticity is considered by performing return mapping on the subspace defined by the plane stress condition. The Hughes–Winget objective integration algorithm is used to handle the finite deformation nonlinear analysis because this integration algorithm provides the consistent tangent stiffness matrix. The meshfree method is used to alleviate the mesh-distortion problems that arise if we use FEM for the finite deformation nonlinear analysis and shape design perturbation during optimization. Since no element information is generated in the meshfree method, the CAD geometry is used to construct curved shell structure. Since the proposed DSA uses the same consistent tangent stiffness as analysis at the converged configuration of each time step, no iteration is required to solve the sensitivity equation. Consequently, DSA takes much less effort than nonlinear response analysis. The accuracy and efficiency of sensitivity information is compared with finite difference results with excellent agreement. It is also demonstrated that optimization can be performed efficiently due to accuracy of the design sensitivity of the continuum-based DSA method.

NOMENCLATURE

$a^{(n+1)}z, \bar{z}$	structural variational form
$a^{*(n+1)}z^k; \Delta z^{k+1}, \bar{z}$	linearized structural variational form
$a'_V{}^{(n+1)}z, \bar{z}$	structural fictitious load form
$C(\xi; \xi - \xi_I)$	correction function
\mathbf{D}	elastic constitutive matrix after enforcing zero normal stress condition
$\bar{\rho}^P$	effective plastic strain
f	yield function
\mathbf{F}	deformation gradient matrix
\mathbf{G}	surface geometric matrix
H	hardening parameter
\mathbf{J}	Jacobian matrix between the physical and parametric coordinate

J_1	Jacobian between configuration t_n and t_{n+1}
\mathbf{l}, \mathbf{m}	surface tangent vectors
$\ell(\bar{\mathbf{z}})$	external load form
$\ell'_V(\bar{\mathbf{z}})$	external fictitious load form
\mathbf{n}	surface normal vector
\mathbf{P}	mapping matrix modified from $\bar{\mathbf{P}}$ in order to account for the factor of two in the shear strain component
$\bar{\mathbf{P}}$	mapping matrix between Cauchy stress and deviatoric Cauchy stress
${}^{n+1}\mathbf{Q}$	global-to-local transformation matrix at configuration t_{n+1}
\mathbf{s}	deviatoric Cauchy stress vector of dimension 5
${}^n\mathbf{V}$	design velocity field at time t_n
\mathbf{z}	displacement field
$\bar{\mathbf{z}}$	virtual displacement
Z	space of kinematically admissible virtual displacement

Greek letters

α	back stress
α'	deviatoric back stress
$\Delta\mathbf{z}$	incremental displacement vector
$\boldsymbol{\varepsilon}$	local strain vector of dimension 5
$\boldsymbol{\varepsilon}^g$	global strain vector of dimension 9
$\boldsymbol{\varepsilon}^l$	local strain vector of dimension 9
$\kappa(\bar{\boldsymbol{\varepsilon}}^p)$	radius of the yield surface
$\boldsymbol{\sigma}$	local Cauchy stress vector of dimension 5
$\boldsymbol{\sigma}^g$	global Cauchy stress vector of dimension 9
$\boldsymbol{\sigma}^l$	local Cauchy stress vector of dimension 9
$\phi_a(\boldsymbol{\xi} - \boldsymbol{\xi}_I)$	kernel function
Ψ_I	meshfree shape function at particle I

ACKNOWLEDGEMENTS

This research is partially supported by General Motors Corporation. This support is gratefully acknowledged.

REFERENCES

1. Botkin ME. Shape optimization of plate and shell structures. *AIAA Journal* 1982; **20**:268–273.
2. Zyczkowski M. Recent advances in optimal structural design of shells. *European Journal of Mechanics and Solids* 1992; **11**:5–24.
3. Yamazaki K, Vandeplaats GN. Design sensitivity analysis with isoparametric shell elements. *Structural Optimization* 1993; **5**:152–158.
4. Gates AA, Accorsi ML. Automatic shape optimization of three-dimensional shell structures with large shape change. *Computers and Structures* 1993; **49**:167–178.
5. Chenis D. Discrete gradient and discretized continuum gradient methods for shape optimization of shells. *Mechanics of Structures and Machines* 1994; **22**:73–115.
6. Csonka B, Kozak I, Mota Soares CM, Mota Soares CA. Shape optimization of axisymmetric shells using a higher-order shear deformation theory. *Structural Optimization* 1995; **9**:117–127.

7. Linby T, Santos JLT. Shape optimization of three-dimensional shell structures with the shape parameterization of a CAD System. *Structural Optimization* 1999; **18**:126–133.
8. Moita JS, Barbosa JI, Mota Soares CM, Mota Soares CA. Sensitivity analysis and optimal design of geometrically non-linear laminated plates and shells. *Computers and Structures* 2000; **76**:407–420.
9. Choi B, Park YH, Choi KK. Shape design optimization of joining mechanism using doubly curved shell. *Computer and Structures* 2000; **77**:495–507.
10. Oral S. A Mindlin plate finite element with semi-analytical shape design sensitivities. *Computers and Structures* 2000; **78**:467–472.
11. Lee SJ, Hinton E. Dangers inherited in shells optimized with linear assumptions. *Computers and Structures* 2000; **78**:473–486.
12. Kim NH, Choi KK, Chen JS, Botkin ME. Meshfree analysis and design sensitivity analysis for shell structures. *International Journal for Numerical Methods in Engineering* 2002; **53**:2087–2116.
13. Simo JC, Taylor RL. A return mapping algorithm for plane stress elastoplasticity. *International Journal for Numerical Methods in Engineering* 1986; **22**:649–670.
14. Simo JC, Kennedy JG. On a stress resultant geometrically exact shell model. part v: nonlinear plasticity: formulation and integration algorithms. *Computer Methods in Applied Mechanics and Engineering* 1992; **96**:133–191.
15. Hughes TJR, Winget J. Finite rotation effects in numerical integration of rate constitutive equations arising in large deformation analysis. *International Journal for Numerical Methods in Engineering* 1980; **15**:1862–1867.
16. Hughes TJR. In *Numerical Implementation of Constitutive Models: Rate-Independent deviatoric Plasticity, Theoretical Foundation for Large-scale Computations of Nonlinear Material Behavior*, Nemat-Nasser S, Asaro RJ, Hegemier GA (eds). Martinus Nijhoff: Dordrecht, 1984.
17. Fish J, Shek K. Computational aspect of incrementally objective algorithms for large deformation plasticity. *International Journal for Numerical Methods in Engineering* 1999; **44**:839–851.
18. *MSC/PATRAN User's Guide*. The MacNeal-Schwendler Corp.: 1999.
19. Chang KH, Choi KK, Tsai CS, Chen CJ, Choi BS, Yu X. Design sensitivity analysis and optimization tool (DSO) for shape design applications. *Computing Systems in Engineering* 1995; **6**:151–175.
20. Bonet J, Wood RD. *Nonlinear Continuum Mechanics for Finite Element Analysis*. Cambridge University Press: Cambridge, 1997.
21. Liu WK, Jun S, Li S, Adee J, Belytschko T. Reproducing kernel particle method for structural dynamics. *International Journal for Numerical Methods in Engineering* 1995; **38**:1655–1679.
22. Chen JS, Pan C, Wu CT, Liu WK. Reproducing kernel particle methods for large deformation analysis of nonlinear structures. *Computer Methods in Applied Mechanics and Engineering* 1996; **139**:195–227.
23. Chen JS, Pan C, Roque CMOL, Wang HP. Lagrangian reproducing kernel particle method for metal forming analysis. *Computational Mechanics* 1998; **22**:289–307.
24. Chen JS, Wu CT, Yoon S, You Y. Stabilized conforming nodal integration for Galerkin meshfree methods. *International Journal for Numerical Methods in Engineering* 2000; **5**:435–466.
25. Chen JS, Wang HP. New boundary condition treatments for meshless computation of contact problems. *Computer Methods in Applied Mechanics and Engineering* 2000; **187**:441–468.
26. Simo JC, Fox MS, Rifai MS. On a stress resultant geometrically exact shell model. Part iii: computational aspects of the nonlinear theory. *Computer Methods in Applied Mechanics and Engineering* 1990; **79**:21–70.
27. Liu WK, Guo Y, Tang S, Belytschko T. A multiple-quadrature eight-node hexahedral finite element for large deformation elastoplastic analysis. *Computer Methods in Applied Mechanics and Engineering* 1998; **154**:69–132.